



# Methane pyrolysis on NiMo/MgO catalysts: The significance of equimolar NiMo alloy resisting nanosize segregation during the reaction

Anita Horváth<sup>a,\*</sup>, Miklós Németh<sup>a</sup>, Andrea Beck<sup>a</sup>, György Sáfrán<sup>b</sup>, Zsolt E. Horváth<sup>c</sup>, István Rigó<sup>d</sup>, Zoltán May<sup>e</sup>, Tamás I. Korányi<sup>a</sup>

<sup>a</sup> HUN-REN Centre for Energy Research, Department of Surface Chemistry and Catalysis, Konkoly-Thege M. Street 29-33, Budapest 1121, Hungary

<sup>b</sup> HUN-REN Centre for Energy Research, Thin Film Physics Department, Konkoly-Thege M. Street 29-33, Budapest 1121, Hungary

<sup>c</sup> HUN-REN Centre for Energy Research, Nanostructures Department, Konkoly-Thege M. Street 29-33, Budapest 1121, Hungary

<sup>d</sup> HUN-REN Wigner Research Centre for Physics, Applied and Nonlinear Optics Department, Konkoly-Thege M. Street 29-33, Budapest 1121, Hungary

<sup>e</sup> HUN-REN Research Centre for Natural Sciences, Institute of Materials and Environmental Chemistry, Plasma Chemistry Research Group, Magyar Tudósok Körútja 2, Budapest 1117, Hungary

## ARTICLE INFO

### Keywords:

Methane pyrolysis  
Nickel  
Molybdenum  
Bimetallic catalyst  
Segregation  
Carbon nanotubes

## ABSTRACT

As a perspective catalyst composition for methane non-oxidative decomposition/methane pyrolysis ( $\text{CH}_4 \rightleftharpoons \text{C} + 2\text{H}_2$ ) yielding clean hydrogen and only solid carbon, the combination of nickel and molybdenum on MgO support was investigated. With deliberately low Ni content and strong metal-support interaction, 7%Ni4% Mo/MgO and 7%Ni12%Mo/MgO catalysts and the monometallic references were prepared. Structural analysis was performed using TPR, XRD, TEM, XPS and Raman spectroscopy in reduced state and after methane decomposition test. Catalytic performance was investigated i) in a highly diluted  $\text{CH}_4$  flow in a fixed bed reactor under temperature ramp and ii) in 50%  $\text{CH}_4/\text{Ar}$  using a horizontal reactor at 800 °C. Synergetic interaction of Mo and Ni was observed under both conditions. The results revealed that the deactivation was coupled with alloy segregation for the low Mo loading, while the more stable, non-segregating Mo/Ni~1 composition of the individual metal particles in 7%Ni12%Mo/MgO sample resulted in good activity and high carbon nanotube yield.

## 1. Introduction

The climate change due to the extreme  $\text{CO}_2$  emission requires the fastest possible transition from fossil to renewable energy sources to fulfill the growing energy consumption of the world. Hydrogen-based economy seems to be a possible solution for our sustainable future. Nowadays industrial scale hydrogen production is done via catalytic steam reforming of methane followed by water-gas shift reaction, but the  $\text{H}_2$  is co-produced with a significant amount of waste  $\text{CO}_2$  ("grey" hydrogen). When most of the  $\text{CO}_2$  is captured during the process, the hydrogen product of the process is called "blue". In contrast, hydrogen obtained from  $\text{H}_2\text{O}$  with renewable energy, for example solar-derived electricity, is named "green", and this is definitely a good way to decrease the carbon footprint of mankind. However, the present-day  $\text{H}_2$  demand as chemical feedstock and energy carrier is far larger than what is available as green hydrogen to us. As an intermediate step for the transition from blue to 100% green hydrogen, a new methane conversion process should be developed and widespread, as the relatively

cheap natural gas and the renewable biogas are still long available.

The so-called methane decomposition/pyrolysis reaction ( $\text{CH}_4 \rightleftharpoons \text{C} + 2\text{H}_2$ ) carried out in an inert atmosphere yields only pure, "turquoise"  $\text{H}_2$  and solid carbon, and if the process heat is provided from renewable electricity, it does not produce waste  $\text{CO}_2$  at all. Beside the environmental issues, the absence of any carbon oxides (especially CO) is compulsory if hydrogen is used in fuel cell applications or for  $\text{NH}_3$  production. Moreover, the solid carbon is considered as a valuable by-product: it can be used as electrodes or additives (in, e.g., concrete, asphalt, tires) or in microelectronics (carbon nanotubes or graphitic fibers). If the market will accept the precious, nanostructured carbon at a reasonable good price, the  $\text{H}_2$  production via methane pyrolysis could compete with steam reforming [1].

The utilization of appropriate catalysts for catalytic decomposition of methane (CDM) can significantly reduce the temperature threshold for the C-H bond breaking. The optimal operating temperature range varies depending on the catalyst type: nickel-based materials are typically investigated in the range of 500–700 °C, iron-based catalysts exhibit

\* Corresponding author.

E-mail address: [horvath.anita@ek.hun-ren.hu](mailto:horvath.anita@ek.hun-ren.hu) (A. Horváth).

<https://doi.org/10.1016/j.apcata.2024.119651>

Received 18 December 2023; Received in revised form 16 February 2024; Accepted 2 March 2024

Available online 4 March 2024

0926-860X/© 2024 The Authors. Published by Elsevier B.V. This is an open access article under the CC BY-NC-ND license (<http://creativecommons.org/licenses/by-nc-nd/4.0/>).

optimal performance in the 700–950 °C range, and carbon-based catalysts are effective around 850–950 °C [2].

Dipu [3] overviewed the recent advancements of Ni-based catalysts and the influence of promoters, metal composition, support, admixture, synthesis method and operating parameters were discussed. Generally, methane conversion increases with Ni loading, but the activity and carbon yield per Ni atom do not usually follow this trend [4]. Fierro et al. [5,6] observed that the graphitization degree of the carbon product is in line with the deactivation of the catalysts. Eventually, depending on the particle size, support nature, reaction condition, Ni-based catalysts lose their catalytic activities due to the carbon layer formation on active metal surfaces [7].

A second metal added to nickel can enhance stability and catalytic activity. The metal modifier is expected to change the nickel properties if sufficient interaction is provided between the two metals (for example, via alloy formation), which can influence the methane cracking rate, carbon migration rate or simply the dispersion of the catalyst and the interaction of metal components with the support [8]. Molybdenum is one of the best candidates to significantly change and possibly improve the methane decomposition properties of the parent nickel catalyst. Molybdenum itself is a good catalyst component under certain conditions and on chosen supports: for example Awadallah et al. [9] produced carbon nanotube bundles with uniform and narrow diameters by using impregnated 20–50% Mo/MgO catalysts at 800 °C from CH<sub>4</sub>. Single phase MgMoO<sub>4</sub> under a H<sub>2</sub>-CH<sub>4</sub> flow resulted also in an extremely high yield of carbon nanotubes at 1000 °C [10,11]. Generally, the catalytic sites for CH<sub>4</sub> activation are suggested to be finely dispersed Mo particles or Mo-carbides (or oxycarbides) formed in situ from the unreduced Mo-oxide component [12–14]. The addition of molybdenum modifier to other metals (Fe [15], Co [16–18]) can be beneficial, but the effect depends – among others – on the Mo content. For example, the use of CoMo/MgO catalyst with high Mo content was not favorable for the production of high-quality carbon nanotubes [16], but in another case the improvement of thermal stability of the catalyst and graphitization degree of MWCNTs was detected upon addition of 25% Mo to a 25% Co/MgO catalyst [18].

As for the mixing of nickel and molybdenum, we found this bimetallic composition very perspective but not too widely investigated within the literature of CDM. Mo addition was mostly investigated from carbon production point of view without deep studies of the catalyst structure and the nanoscale reasons for the different performance compared to nickel. We should note that beneficial or synergetic effect of Mo as additive to nickel was observed too in cases when instead of methane, other carbon sources such as ethylene [19,20] or polypropylene [21–23] were used. Usually the Mo loading was high, comparable with that of the support [24], and catalysts were not prerduced in hydrogen prior to the methane pyrolysis test [24,25]. Thus, the structural info presented about the calcined state of the catalyst does not inform us about the working state under the reducing atmosphere of methane decomposition. Extremely high carbon yield was obtained over a platelet-structured catalyst: the sol-gel derived Ni-Mg-oxide paste was mixed with Mo powder, ground fine and calcined at different temperatures yielding low Ni-loaded samples (Mo/Ni=30, Mo/Mg=2.7) [24]. The possibility of NiMo alloy formation during reaction was not suggested, but separate Mo<sub>2</sub>C and Ni<sub>3</sub>C particles were supposed to govern the carbon diffusion and the typical base growth of MWCNT bundles strongly attached to the catalyst fragments [24]. Awadallah et al. [20] investigated the effect of 1% Mo (among Cr and W) on 4%Ni/MgO catalyst and observed a threefold increase in the carbon yield (87%) compared to the parent Ni catalyst in CVD of ethylene at 850 °C, but the reaction mechanism for the increased nanotube formation was not brought up. The RSM one factor design method [21] was applied to study the effect of Ni/Mo mole ratio on the carbon yield of calcined NiMo/MgO catalysts using polypropylene carbon source, and the Ni/Mo mole ratio of 20 (Mo/Ni=0.05, low Mo content) was found to be optimum. Higher Mo content led to lower yield and large diameter CNTs,

but Mo distribution inside the catalyst components was not investigated. Li et al. [26] reported formation of MWCNT bundles with a very high yield over a Ni/Mo/MgO (0.1/1.2/1.0) catalyst from a CH<sub>4</sub>-H<sub>2</sub> source at 1000 °C. The synergism of Ni and Mo was explained by assuming the accelerated diffusion of carbon atoms assisting the growth of nanotubes. Interestingly, XRD detected the transformation of MoO<sub>3</sub> and MgMoO<sub>4</sub> to Mg<sub>2</sub>Mo<sub>3</sub>O<sub>8</sub> and Mo in the fresh, reduced sample and the presence of graphite, MgO and MoC in the spent one. The very nice paper of Nakamura et al. [27] gained deeper insights into the reduced form of different Ni/Mo/MgO catalysts before/after the methane dissociation and gave precious reasoning on the role of Mo and the synergetic effect. In the above paper either Mo or Ni mole fraction was fixed during preparation from the paste of nitrate salts and citrate. The catalyst samples reduced at 650 °C were analyzed by TEM and XRD. The results showed that particle size became larger with increasing Mo mole fraction, and the distribution became broad (at Mo/Ni=0.5 ratio the particle size was in the range of 1.5–8 nm). XRD for Mo mole fractions over 0.1 detected a NiMo alloy peak that was Ni rich then turned into Mo rich with increasing the Mo content. XRD of the spent samples suggested NiMo alloy segregation into Mo<sub>2</sub>C and Ni (or Mo-including Ni). As for the reaction mechanism, they concluded that Ni is responsible for the dissociation of CH<sub>4</sub> into carbon and Mo<sub>2</sub>C works as a carbon reservoir.

After this short review of the most relevant results about different Ni-Mo-MgO systems being active in methane (and other hydrocarbons) pyrolysis, we should point out the novelty of our upcoming work. It is clear that upon addition of Mo to Ni one can expect a synergetic effect in carbon formation ability. However, except of the work of Nakamura, most papers stay at this point and just vary the Mo content and quantify the amount and the purity of the deposited carbon by TG and Raman measurements. We would approach the question from the perspective of catalyst structure just prior to the CH<sub>4</sub> contact, when the metals are (partially) reduced. We applied a simple commercial MgO support, low Ni and two different low Mo contents and a special synthesis route to induce strong metal-support interaction. NiMo/MgO catalyst was chosen because of environmental issues as well: all the components can be dissolved in acid and so pure nanocarbon can be obtained after the reaction, if needed. Surface sensitive XPS technique was used to provide information about the reduced catalyst surface and HRTEM and STEM-EDS delivered the nanoscale picture of NiMo particles existing before and after the reaction. Detailed XRD analysis was applied to estimate the composition of NiMo alloys when it was possible. TPR and Raman experiments were also inevitable to explain the results. As for the activity of different NiMo surfaces, the results of temperature ramped CH<sub>4</sub> decomposition experiments were coupled with pyrolysis tests in a commonly applied horizontal reactor. Our aim was to give the reasons for the synergetic activity by the in-depth study of the reduced and spent catalyst structure. The three most important novelties of our work were i) the meticulous evaluation of the reduced catalyst structure containing nanosize NiMo alloyed particles via XRD reflections and STEM-EDS derived elemental maps before and after the catalytic reaction; (ii) the detailed quantitative analysis of the carbon products by Raman spectroscopy; and finally iii) the disclosure of the hindered segregation of the Ni:Mo~1:1 alloy particles producing the least amount of deactivating amorphous carbon leading to superiority in carbon yield compared to other cases that are Ni rich.

## 2. Experimental

### 2.1. Catalyst preparation

Commercial Merck MgO (extra pure, 72 m<sup>2</sup>/g BET surface area, 13.9 nm average pore size) was used as a support. 0.2 M precursor solutions of Ni(NO<sub>3</sub>)<sub>2</sub> × 6 H<sub>2</sub>O (Aldrich, 99.999%) and (NH<sub>4</sub>)<sub>6</sub>Mo<sub>7</sub>O<sub>24</sub> × 4 H<sub>2</sub>O (Sigma-Aldrich, 99.98%) were added to the aqueous suspension of MgO dropwise, one after the other in calculated amounts as signed in Table 1. The pH of the suspension was around 10–11. The final volume

**Table 1**

Preparation details, metal content and particle size of the samples.

Sample name	Added 0.2 M precursors (mL)		Metal loading by ICP (wt%)		Mo/Ni atomic ratio	fresh $d_{\text{TEM}}$ calc/red state (nm)	spent $d_{\text{TEM}}$ after $\text{CH}_4/800^\circ\text{C}$ (nm)
	Ni	Mo	Ni	Mo			
Ni	5.96	-	7.5	-	-	5.0±1.2	4.4±1.2
Mo	-	11.93	-	13.0	-	6.5±2.9	5.5±2.0
MoNi0.4	5.96	2.39	6.3	4.2	0.4	7.9±2.7	6.0±3.6
MoNi0.4_RT	5.96	11.93	8.0	5.1	0.4	8.1±3.9	8.1±5.7
MoNi1.2	5.96	11.93	6.5	12.4	1.2	7.1±3.4	6.3±3.5

of the suspension was 60 mL in all cases. As for the room temperature preparation, the mixing of all components was maintained for 60 min, while for the rest of the samples, the suspension was heated to 80 °C and kept there for 1 h. After this 1 h isothermal hold step (and cooling in the case of 80 °C synthesis) the supernatant was removed and 3 cycles of centrifuging and washing followed. The color stability of the solid phase ascertained that washing with 3×20 mL of water did not remove the Ni component. Finally, samples were dried at 80 °C for 1 day and calcined in synthetic air flow at 550 °C for 1 h (after heating up with 10 °C/min). Reduction step in hydrogen atmosphere at 800 °C for 1 h was done prior to the XPS, TEM, XRD and catalytic experiments. The annotation of the samples (see in Table 1) contains the real Mo/Ni elemental ratio obtained by ICP-OES method and the “RT” denotes the synthesis carried out at 25 °C.

## 2.2. Structural investigations

ICP-OES. For elemental analysis of the calcined samples 25 mg portions were weighed with analytical balance into glass beakers and then 8 mL of inverse aqua regia (5 mL of 67% nitric acid and 3 mL of 37% hydrochloric acid) was added to them. The solid samples were completely dissolved during a night in ambient temperature. Blank solution was prepared as well. The sample solutions were completed up to 50 mL with ultrapure water (18.2 MΩ/cm) into volumetric flasks. Solutions obtained by this procedure were measured with ICP-OES (Spectro Genesis inductively coupled plasma optical emission spectrometer, Kleeve, Germany, a simultaneous spectrometer operating with axial plasma observation).

$\text{N}_2$  adsorption measurements. Low temperature (-196.15 °C) nitrogen adsorption measurements were performed on the calcined and reduced monometallic and MoNi0.4 bimetallic catalysts after 24 h degassing at 250 °C on a NOVA 2000e (Quantachrome, USA) instrument. The specific surface area (SSA) was determined using the Brunauer-Emmett-Teller (BET) model. The pore volume  $V_p$  was estimated from the amount of vapor adsorbed at  $p/p_0 = 0.95$ .

Temperature Programed Reduction (TPR). The reducibility of the calcined samples was studied by TPR in two experiments up to 800 °C and 1000 °C with 60 and 30 min isothermal period at the end, respectively, in an Autochem 2920 (Micromeritics) instrument using thermal conductivity detector. 50 mg of each calcined samples were in situ pretreated in 10%  $\text{O}_2/\text{He}$  flow (30 mL/min) at 400 °C for 30 min, then after cooling down in Ar the TPR was performed in 10%  $\text{H}_2/\text{Ar}$  (30 mL/min) with 10 °C/min heating rate.

X-Ray Diffraction (XRD). To study the crystalline phases in the catalysts in different states (calcined, calcined/reduced, after catalytic tests) XRD measurements were carried out with a Bruker AXS D8 Discover X-ray diffractometer equipped with Göbel-mirror and scintillation detector using  $\text{Cu K}\alpha$  ( $\lambda=1.5406$  Å) radiation. The X-ray beam

dimensions were 1 mm \* 5 mm, the  $2\theta$  step size was 0.02°, scan speed 0.12°/min.

Raman spectroscopic measurements were performed utilizing a Renishaw InVia micro-Raman spectrometer. We employed a 532 nm (2.33 eV) laser for the excitation. The laser beam was precisely focused into a spot with a diameter of approximately 1 μm. Each measurement had an integration time of 10 seconds. Multiple spectra were acquired from each sample. To enhance the data quality, the spectra underwent baseline correction and fitting procedures using Gaussian functions for broad bands and Lorentzian functions for narrow peaks.

Transmission Electron Microscopy (TEM). A FEI Titan Themis 200 kV spherical aberration (Cs) - corrected TEM with 0.09 nm HRTEM and 0.16 nm STEM resolution equipped with 4 Thermofischer EDS detectors was applied for investigation of the morphology and composition of the calcined/reduced catalysts and those used in methane pyrolysis. Composition of the samples was measured by STEM-EDS along with the recording of HAADF (high-angle annular dark-field) images on selected areas. The data were evaluated and elemental maps were created by using the Velox software.

X-Ray photoelectron spectroscopy (XPS). To determine the composition and chemical state of the catalyst surface, XPS measurements were performed in a KRATOS XSAM 800 instrument equipped with an atmospheric pretreatment chamber and using an unmonochromatized Al K-alpha source (1486.6 eV). The Ni 2p, Mo 3d, Mg 2p, O 1s and C 1s binding energy regions were recorded first on the ex situ calcined sample, then after an in situ reduction at 800 °C in hydrogen flow for 1 h. The Mg 2p binding energy from the magnesia support set at 50.0 eV was used as reference for charge compensation.

## 2.3. Catalytic investigations

The methane decomposition was studied in two experimental setups. With 1%  $\text{CH}_4/\text{He}$  reactant mixture, temperature programmed (TP) measurements between 200 and 800 °C with 10 °C/min heating rate were performed in a Micromeritics Autochem 2920 instrument with QMS (ThermoStar) analysis. 20 mg of calcined catalysts were in situ reduced at 800 °C for 1 h in 10%  $\text{H}_2/\text{Ar}$ . After cooling in He to 200 °C for the TP reaction, 1%  $\text{CH}_4/\text{He}$  was added with a 30 mL/min flow rate. During the reaction the ion current of the  $m/e=2$  ( $\text{H}_2$ ), 15 ( $\text{CH}_4$ ) fragments were recorded together with that of  $m/e=4$  for He. The resulting  $\text{CH}_4$  conversions were calculated.

Pyrolysis tests at 800 °C with a 50%  $\text{CH}_4/\text{Ar}$  reactant mixture were carried out in a horizontal quartz reactor tube of 1 cm inner diameter and 15 cm length in the isothermal part of a furnace. 50 mg of each calcined catalyst was placed in a quartz vessel in the middle of this tube and reduced in situ at 800 °C in hydrogen flow (30 mL/min) for 1 h. After a 5 minute Ar purge, the methane decomposition was started by switching to 60 mL/min 50%  $\text{CH}_4/\text{Ar}$  flow. The reaction was allowed to proceed for 180 min or until there was no more  $\text{H}_2$  evolving. Gas phase samples were taken from the outlet flow after 1 minute and in every 20 minutes and analyzed by a gas chromatograph equipped with CarboPLOT P7 fused silica column and TCD detector operating with an 8.5%  $\text{H}_2/\text{He}$  carrier gas. Only  $\text{H}_2$  was detected as gas phase product. The concentration of  $\text{CH}_4$ ,  $\text{H}_2$  and Ar was determined based on calibration measurements. Supposing that the methane decomposition is the only transformation, the following equation was used to calculate conversion of methane ( $X_A$ ):

$$X_A = \frac{1 - C_A/C_{A0}}{1 + \alpha * C_A/C_{A0}}$$

where  $\alpha=0.5$  is the expansion factor under our conditions,  $C_A$  and  $C_{A0}$  are the actual and initial concentrations of  $\text{CH}_4$ , respectively. At the end of the reaction, the gas flow was changed to argon and the reactor was cooled down, then the weight increase was measured to determine the amount of the solid carbon product. Carbon production was calculated

from the methane conversion data as well.

### 3. Results and discussion

#### 3.1. Investigation of calcined samples: metal loading, XRD, Raman and TPR

During sample preparation, Ni precursor solution was added first, followed by the immediate dropwise addition of Mo precursor to the aqueous suspension of MgO at room temperature. Then, the suspension was either kept at 25 °C (RT) for 1 h or heated to 80 °C and kept there for 1 h. Table 1 collects the important parameters of sample preparation and the real metal loadings determined by ICP-OES together with particle sizes (will be discussed later). The final Ni concentrations in calcined state were close to the planned 7 wt% value (in reduced state) independent of the synthesis temperature. Indeed, the fast greenish coloring of the suspended support showed us the sufficient adsorption (and precipitation) of  $\text{Ni}^{2+}$  on the MgO surface. As for the Mo deposition, compared to the theoretical 23% Mo loading (achievable with 11.93 mL Mo precursor solution), much less Mo loading was obtained. Only ~13 wt% Mo could be loaded onto the MgO support with a very strong interaction that was maintained after the 3 cycles of washing and centrifuging. Interestingly, this amount was independent of the presence of Ni compound (as the same Mo content was obtained for Mo and MoNi1.2 samples), but was drastically influenced by the synthesis temperature in favor of 80 °C versus RT (MoNi0.4\_RT). Based on this experience, the same Mo loading as of the MoNi0.4\_RT sample (~5 wt %) was attempted to get with 80 °C synthesis to have an analogous sample. Fortunately, the attempt was successful (resulting MoNi0.4 sample). The Ni and Mo loadings are not exactly the same for MoNi0.4 and MoNi0.4\_RT, but they are very close, and the Mo/Ni ratio is the same. Thus, any differences experienced between these two samples will be derived from the different synthesis conditions. The limitation of Mo loading over the basic MgO support must originate from the limited number of positively charged adsorption sites of MgO that are able to strongly bind the  $\text{MoO}_4^{2-}$  species at pH values around 10. This number must be higher at 80 °C than at room temperature, as point of zero charge of the support is expected to increase with temperature [28]. Apparently, the less Mo precursor to get Mo/Ni=0.4 ratio was successfully attached to MgO at 80 °C (the real and the theoretical Mo loading accorded).

Our preparation conditions allow that the MgO surface could be partially dissolved during the adsorption-precipitation procedure, especially at higher temperature, because the hydration rate and the MgO dissolution (also the  $\text{Mg}(\text{OH})_2$  precipitation) is expected to increase with temperature [29]. Thus, one might expect some change in the textural properties of the catalysts compared to the parent MgO. Then, an additional change could happen due to the calcination/reduction treatment when most of the metal precursor ions get reduced and form alloy particles. Specific surface area (SSA) and the pore volume of chosen calcined and reduced catalyst samples are presented in Table S1. The Mo addition alone resulted about the same SSA value as that of the parent MgO without the high temperature treatments (72  $\text{m}^2/\text{g}$ ). This is possible only if Mo introduction stabilizes the MgO structure that would otherwise definitely sinter at the high temperature calcination/reduction. MoNi0.4 catalyst showed a 40% increase and the highest SSA increase (60%) was obtained for the monometallic Ni sample (112  $\text{m}^2/\text{g}$ ) after the reduction treatment when most part of nickel becomes metallic. This suggests a deeper hydration in the presence of Ni precursor and a stronger metal-support interaction.

X-ray diffractometry was applied to analyze the calcined samples. Nothing but the MgO peaks were discerned. The low calcination temperature of 550 °C and the relatively low Mo and Ni loading could also be responsible for the absence of any NiO,  $\text{MoO}_3$ ,  $\text{NiMoO}_4$  or  $\text{MgMoO}_4$  lines [9,17]. The only difference between the samples was the asymmetry of the MgO peaks at  $2\theta = 36.9^\circ$ ,  $42.8^\circ$ ,  $62.2^\circ$  (JCPDS 89-7746) for

the samples with ~13 wt% Mo (see Fig. S1). The fitting of those peaks (Fig. S1) resulted beside the “normal lattice” (4.22 Å) parameter, a higher value component of 4.26 Å and 4.25 Å for the calcined Mo and MoNi1.2 samples, respectively (see Table S2). This means that the Mo-oxide addition induced a significant MgO lattice restructuring and inclusion of Mo into the framework of the support and did not result in agglomeration of  $\text{MoO}_3$  on the surface. Awadallah et al. on calcined 5% Ni11%Mo/ $\text{Al}_2\text{O}_3$  sample [25] found only NiO and no  $\text{MoO}_3$  compounds by XRD, while over 4%Ni1%Mo/MgO catalyst [20] only the support peaks. When MgO component was significantly less than here (viz. higher Mo and Ni loading), it was possible to detect the presence of crystalline  $\text{MgNiO}_2$ ,  $\text{NiMoO}_4$ , and  $\text{MoO}_3$  over catalysts prepared by combustion method [22,26].

We also employed Raman spectroscopy to gain further insights into the Mo distribution and coordination geometry of samples with high Mo content. According to Wachs and his co-workers [30], oxide supports possessing a basic pH in their suspensions at point of zero charge (PZC) such as MgO exhibit a preference for the formation of tetrahedrally coordinated, monomeric species like  $\text{MoO}_4^{2-}$  regardless of the pH of the impregnating solution. These species can be detected by Raman spectroscopy. For our Mo sample, peaks at 319 and 913  $\text{cm}^{-1}$  with shoulders at 813 and 859  $\text{cm}^{-1}$  were seen (Fig. S2) and could be assigned to the tetrahedral molybdenum monomers, because Raman bands at higher wavenumbers (above 930–970  $\text{cm}^{-1}$ ) would sign the octahedrally coordinated polymolybdate species, but those were absent. Molybdenum oxide monolayer is composed of distorted octahedrals and would result bands well above 900  $\text{cm}^{-1}$ , or crystalline  $\text{MoO}_3$  species would give peak at around 996  $\text{cm}^{-1}$  – these were not detected [31]. The small peak at 447  $\text{cm}^{-1}$  is assigned to  $\text{Mg}(\text{OH})_2$  [32,33]. This means, the 13 wt% Mo of our monometallic sample is well dispersed in/on the hydrated MgO surface. In Fig. S2 the MoNi1.2 sample showed peaks at 283, 340, 361, 849, 898 and 948  $\text{cm}^{-1}$ : these are assignable to  $\text{MgMoO}_4$  [30] and a probably distorted tetrahedral  $\text{NiMoO}_4$  [34,35], but the hydrated MgO peaks were absent. The nickel component definitely interacts with molybdenum species and due to the ~7% nickel loading, the hydroxyls of MgO are used up.

Next, reducibility of the calcined samples will be discussed based on the TPR experiments. The quantification of the TPR curves are listed in Table S3. Two types of experiments were done: temperature was ramped up to 800 °C or to 1000 °C with a 60 or a 30 min hold time, respectively. Note that for the catalytic and other structural characterizations, we set a reduction pretreatment at 800 °C for 1 h not to sinter the catalysts needlessly, because the  $\text{H}_2$  consumption of all the bimetallic catalysts corresponded to reduction degree of 100% already with the 800 °C reduction method. However, the monometallic samples were not completely reduced: Ni sample achieved 71% reduction degree at 800 °C and 77% at 1000 °C, while these values for Mo sample were 46 and 82%, at 800 and 1000 °C respectively. Fig. 1 depicts the TPR curves obtained during TPR to 1000 °C. The calcined Ni sample had some easily reducible surface NiO species (peak at 365 °C), but most NiO was in strong interaction with MgO, probably in the form of a mixed MgO-NiO oxide (peak maximum at 780 °C) that was not completely reducible even up to 1000 °C in accordance with the literature [36]. The well dispersed tetrahedral Mo(VI) centers of Mo sample were reduced at 703 °C to  $\text{Mo}^0$  or Mo(IV), but most of the Mo(IV) inside the MgO structure or as surface  $\text{MoO}_2$  species were reduced to metal only at 912 °C. These latter Mo(IV) species did not transform into metallic form when using the 800 °C reduction treatment (remember the only 42% reducibility) in agreement with the results over a 9.5%Mo/MgO sample reported by Bahmani et al. [37].

To evaluate the bimetallic samples, it should be noted that bulk  $\text{NiMoO}_4$ , if Mo(VI) is in octahedral position ( $\alpha\text{-NiMoO}_4$ ), is easier to reduce than the  $\beta$  counterpart where Mo(VI) is tetrahedrally coordinated [38]. Furthermore, presence of extra Ni can stabilize the  $\beta\text{-NiMoO}_4$  at room temperature (it is basically a high temperature form of  $\text{NiMoO}_4$ ) [38]. Catalyst sample MoNi1.2 having about the same number of oxidic



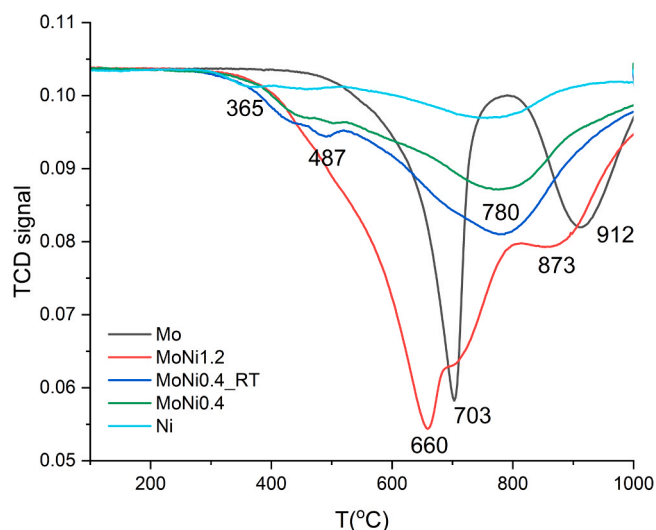


Fig. 1. TPR curves of the calcined samples.

Mo and Ni atoms started the reduction process at around 350 °C, and the maximum of the curve at 660 °C is assignable to the reduction of beta (tetrahedral)  $\text{NiMoO}_4$  with a high temperature shoulder at 703 °C of  $\text{MgMoO}_4$ , while the last overlapped peak component at 873 °C could mean amorphous  $\text{MoO}_2/\text{Mo(IV)}$  species [39,40] that are easier to reduce here than in the reference Mo catalyst because of the presence of metallic Ni and NiMo particles. In the case of samples with low Mo content, the TPR curves were very similar: NiO reduction started above 300 °C and spread over a wide range of temperature with a small local maximum at around 487 °C and curve maximum at 780 °C corresponding to the reduction of a mixed  $\text{NiO-MoO}_x\text{-MgO}$  phase where the reduced Ni/NiMo accelerates the reduction of  $\text{MoO}_x\text{-MgO}$  having very different coordination geometry and location. As there are no separable peak components, it is hard to distinguish between any  $\text{MgMoO}_4$  or  $\text{NiMoO}_4$  surface species here.

### 3.2. Investigation of the calcined/reduced samples before the reaction: XRD, (HR)TEM, STEM-EDS and XPS analysis

After all information about the oxidized samples, we will turn to the calcined 550 °C/reduced 800 °C state that was present right prior to the catalytic tests. Very few works report the XRD measurement of reduced samples, but we got to know that for example a  $\text{Ni}_{0.1}/\text{Mo}_{1.2}/\text{MgO}_{1.0}$  catalyst after a 700 °C reduction by  $\text{H}_2$  exhibited  $\text{Mg}_2\text{Mo}_3\text{O}_8$  and Mo peaks [26] (because of the transformation of  $\text{MgMoO}_4$  and  $\text{MoO}_3$  crystalline components). Note, that our catalyst preparation method (not combustion as usually) and catalyst composition is completely different ( $\text{MgO}$  is in dominance). When Ni and Mo molar fraction is not higher than 0.05, only the diffractions peaks of  $\text{MgO}$  were detected according to Nakamura and his co-workers [27]. For our  $\text{MoNi}_{1.2}$  sample the ratio of the 3 components are about  $\text{Mo}_{0.06}\text{Ni}_{0.05}\text{Mg}_{0.89}$ . Indeed, XRD patterns in Fig. 2 show that only  $\text{MgO}$  peak is present for  $\text{MoNi}_{1.2}$ .

The other two bimetallic samples have tiny peaks shifted to lower  $2\theta$  values from the Ni position and so they can be attributed to NiMo alloy particles. Mo atoms are larger than Ni atoms, therefore the introduction of the former into the crystal lattice of Ni should result in the growth of a lattice parameter [41]. The peak asymmetry and shift mean that different NiMo alloy compositions and also particle sizes exist within the catalyst. After precise fitting of the Ni (200) peak at around  $52^\circ$  2theta, we obtained the details of XRD evaluation. According to these results in Table S4, in both  $\text{MoNi}_{0.4}$  and  $\text{MoNi}_{0.4\_RT}$  samples there are larger sized (roughly 20 nm) NiMo fraction with less, 14–23% Mo content and a smaller sized fraction ( $\sim 5$  nm) with around 30% Mo content. The smaller crystallites are more numerous in  $\text{MoNi}_{0.4}$  than in the

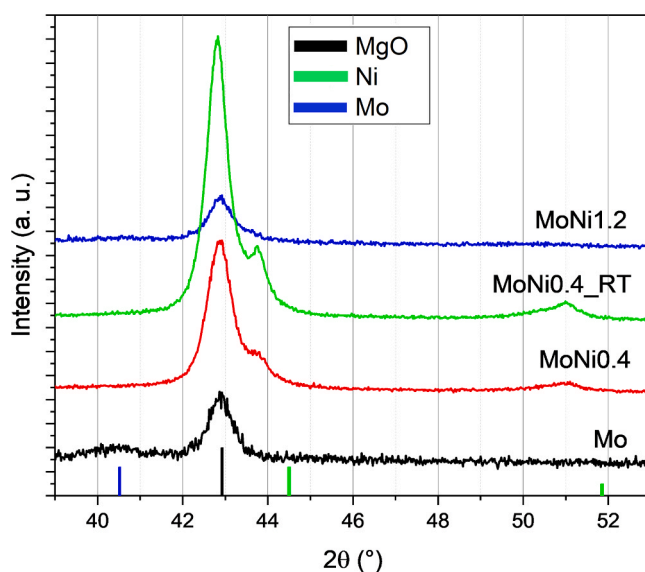


Fig. 2. XRD pattern of the calcined/reduced catalysts. Vertical lines are those of references (black:  $\text{MgO}$ , green: Ni, blue: Mo).

counterpart sample produced at room temperature ( $\text{MoNi}_{0.4\_RT}$ ). Actually, according to the phase diagram of Ni and Mo alloy at low Mo fraction,  $\text{Ni}_3\text{Mo}$  and  $\text{Ni}_4\text{Mo}$  intermetallics can exist beside the solid solution of nickel and molybdenum. The low intensity XRD peaks do not allow to distinguish any intermetallic compound in our case. The most important outcome is that Mo distribution among the Ni particles is size dependent and surely not homogeneous. As for the pure Mo catalyst, a weak peak at  $40.5^\circ$  signs the presence of crystalline Mo metal of about 6.5 nm size. Again, the bimetallic sample with high Mo content having no XRD reflections in reduced state must have high dispersion of NiMo (particles smaller than 5 nm).

TEM/HRTEM and STEM-EDX measurements were carried out to further clarify the catalyst morphology with special attention to the distribution of the two metals (Figs. 3–5 and Figs. S3, S4). This kind of investigation is very rare in the literature, to the best of our knowledge, we are the first to provide such detailed TEM analysis about the nanoscale environment of supported and reduced Ni-Mo catalysts used for pyrolysis ever.

The monometallic Ni catalyst in Fig. S3 possesses a very nice, homogeneous distribution of metal particles with small average particle size of 5 nm as shown in Table 1. Similarly, the Mo sample has nicely spread particles of 6.5 nm with somewhat wider distribution or more irregular shape as can be seen in Fig. 3a. The STEM-EDS image helps to spot Mo particles, but Mo signal can be seen also in the  $\text{MgO}$  support reflecting the hard reducibility of this sample and suggesting that Mo is present in the oxide phase. The “empty” area (only support area) framed in Fig. 3b resulted  $\text{Mg}/\text{Mo} \sim 22$  ratio. The HRTEM image in Fig. 3c indicates the lattice fringes of metallic Mo (110) with line spacings of 0.22 nm.

Fig. 4a–d represents the TEM results of  $\text{MoNi}_{0.4\_RT}$ . Apparently, the dark spots of metallic particles have the widest size distribution ( $8.1 \pm 3.9$  nm) as seen in Fig. 4a and Table 1. The STEM-EDS image in Fig. 4b reveals the Ni particles (in green) and the Mo distribution (in red): note that Mo signals were detected not only together with Ni but separately in the  $\text{MgO}$  support as well. The framed area gave a  $\text{Mg}/\text{Mo} \sim 60$  ratio (bulk would be 34) with high uncertainty in Mo content due to the low signal intensity. This means molybdenum (oxide) can be found in  $\text{MgO}$  where metallic Ni is absent. The places with densely packed Ni particles provided  $\text{Mo}/\text{Ni} \sim 0.17$ , while larger particles had  $\text{Mo}/\text{Ni} \sim 0.12$  in average. Fig. 4c shows the STEM-EDS map of a single large alloy particle with  $\text{Mo}/\text{Ni} = 0.12$  and its HRTEM image in Fig. 4d with lattice spacings of 0.207 nm, proving the presence of both metals in a single particle with

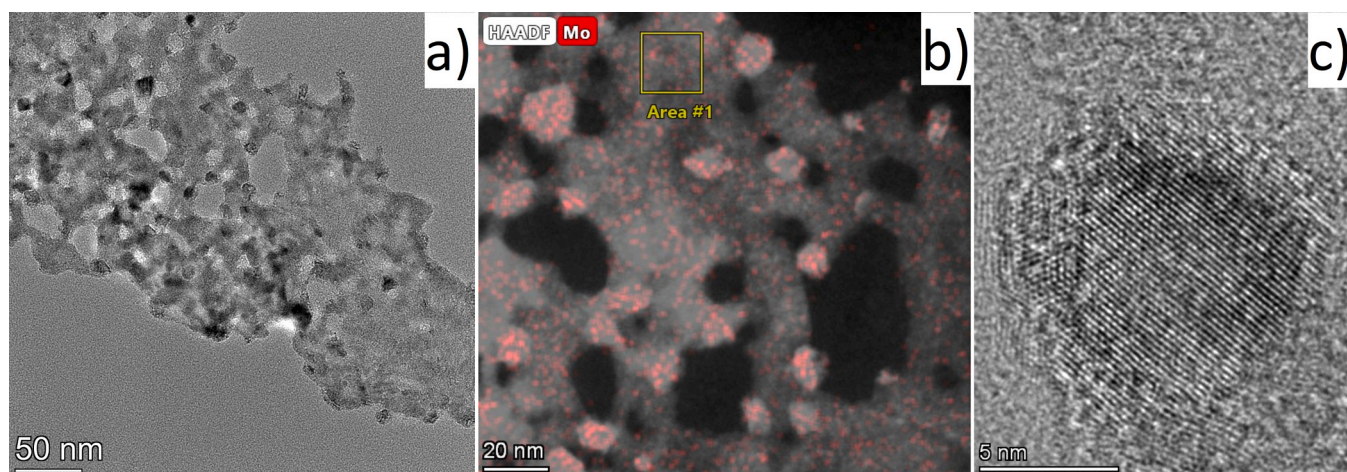


**Fig. 3.** Representative images of the calcined/reduced Mo catalyst: (a) TEM; (b) HAADF with STEM-EDS elemental map of Mo with a framed “empty” support area where Mg/Mo~22; (c) HRTEM of a single Mo particle with line spacings of 0.22 nm.

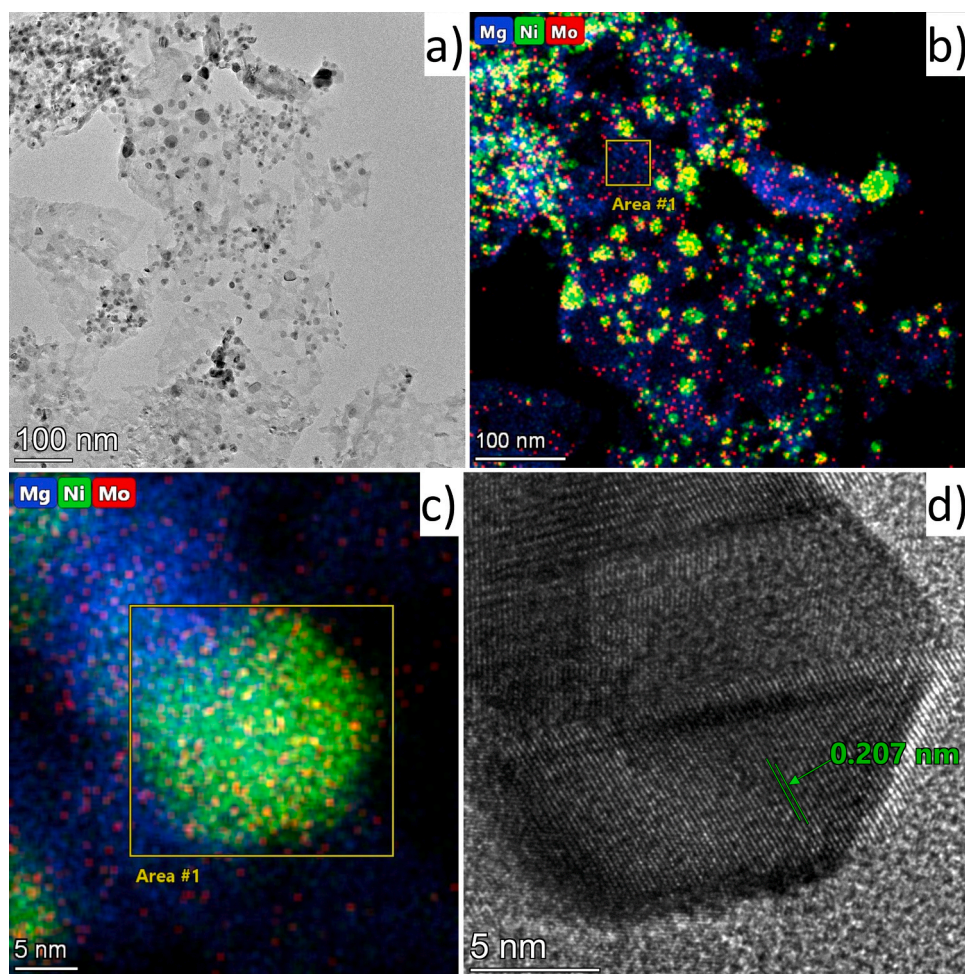


**Fig. 4.** Representative images of the calcined/reduced MoNi<sub>0.4</sub> RT catalyst: (a) TEM; (b) STEM-EDS elemental maps of Mg, Ni and Mo with a framed “empty” support area where Mg/Mo~60; (c) STEM-EDS elemental maps of Mg, Ni and Mo over a single 19 nm size particle with Mo/Ni=0.12; (d) HRTEM image of the same particle with line spacings of 0.207 nm.

the majority of Ni component (Ni-rich alloy). Remember, the XRD peak fitting resulted for the largest 21 nm sized particle fraction 14% Mo in the Ni lattice ( $a=3.577 \text{ \AA}$ ) which is exactly what we can see here as 0.207 nm lattice spacings. The corresponding separated elemental maps are collected in Fig. S4.

The counterpart with the same metal loading, MoNi<sub>0.4</sub> sample prepared with the 80 °C synthesis method is shown in Fig. S5. The nicer and more homogeneous distribution of particles is evident in Fig. S5a ( $7.9 \pm 2.7 \text{ nm}$ ). The STEM-EDS map in Fig. S5b revealed that large particles again were richer in Ni (Mo/Ni~0.17), while areas with dense, smaller



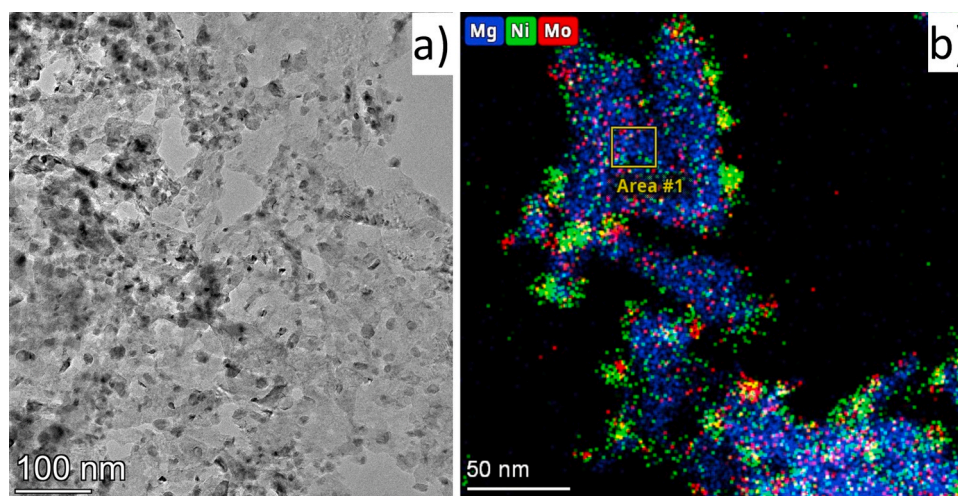


**Fig. 5.** Representative images of the calcined/reduced MoNi1.2 catalyst: (a) TEM image; (b) STEM-EDS elemental maps of Mg, Ni and Mo with a framed “empty” support area where Mg/Mo~15.

particles provided an average Mo/Ni~0.24 value (corresponding to the composition of Ni<sub>4</sub>Mo phase). Remember, XRD peak fitting resulted that small, ~5 nm particles are in majority with 27% Mo content. The empty support area (Area#1) had Mg/Mo~80 value meaning that separated Mo was less than in MoNi0.4\_RT. Thus, sample prepared with the higher synthesis temperature could group Mo and Ni component more intimately.

Finally, the bimetallic MoNi1.2 sample with the higher Mo content is depicted in Fig. 5. The general TEM image in Fig. 5a shows a nice distribution of darker spots signing metallic particles on MgO with an average size of  $7.1 \pm 3.4$  nm. A STEM-EDS map in Fig. 5b proves the enrichment of Mo where Ni particles are present, however, in the empty area with Mg/Mo~15 there was some Mo (and Ni) present separately (the separated elemental maps of Mg, Ni and Mo are shown in Fig. S6). The distribution of Mo and Ni in each particle was not completely even, but in the smaller particles a Mo/Ni~0.94 value was detected on average, while in larger particles (~10 nm) we measured Mo/Ni~0.45 ratio. Note, that this latter number is still higher than what was present in the Mo-richer small particles of the other two bimetallic samples. To summarize the TEM results, all samples have particle size below 10 nm, but the size distribution widens with the introduction of Mo compared to the reference Ni catalyst and the synthesis at 80 °C resulted in more intimate contact of Ni and Mo species.

XPS analysis was conducted on the calcined samples, then right after a reduction treatment at 800 °C in H<sub>2</sub> carried out in situ in the pre-treatment chamber of the instrument. This assembly avoids the air contact of freshly reduced surface. Table 2 includes all the most important XPS data obtained and Fig. 6 contain the XPS curves taken for Ni 2 p and Mo 3 d region after the in situ reduction treatment. Curve fitting for these spectra can be seen in Fig. S7 separately.

For all the calcined samples the Ni 2p<sub>3/2</sub> peak was situated at 856 eV

(not shown) that is much higher than the standard 853 eV of bulk NiO. This means Ni<sup>2+</sup> is in a very strong interaction with the MgO and/or Mo-Mg oxide: embedded in the (surface) matrix of the support in accordance with the TPR, Raman and XRD measurements. All Mo 3d<sub>5/2</sub> peaks were detected at 233 eV typical of Mo(VI) BE. As for all Ni-containing calcined samples, the surface Ni concentration was similar (reflected in Mg/Ni), expect for MoNi0.4 where it was obviously higher and this tendency remained the same upon reduction. This means a Ni enrichment of the surface of MoNi0.4. The cause of this phenomenon should be related to the deposition procedure of Ni and Mo precursors during the preparation, particularly within this concentration range, but the details should be further studied separately.

The process of reduction, which converts dispersed oxides into metallic particles, inherently induces a decrease in surface concentrations of nickel and molybdenum, leading to an elevation in Mg/Me ratios. Furthermore, this process may give rise to segregation or mixing of metals, thereby potentially modifying the Mo/Ni ratio relative to the calcined state. Thus, the best is to compare the samples with the same bulk Mo loading when interpreting the findings. MoNi0.4 and MoNi0.4\_RT differ in the somewhat higher bulk concentration of Ni and Mo for the latter catalyst (Table 1). Upon reduction, Ni sinters more in MoNi0.4\_RT sample, this is why the Mo/Ni ratio is double compared to MoNi0.4 (and corresponds to the theoretical bulk value). Interestingly, nickel is completely in zero oxidation state in these two samples, but molybdenum is partially oxidized (in contrast to the TPR results), having both Mo(VI) and Mo(IV) according to the XPS fitting results listed in Table 2 (see Fig. S7 as well). As XPS is sensitive to a few nm thick top layer of catalysts, this means that MoO<sub>x</sub> species must be present and enriched in the surface layer and such oxidic Mo are with 10% more in number in MoNi0.4\_RT (only 55% is metallic). At the higher Mo-loading, Mo reduction degree is higher (~72 and ~79% for MoNi1.2

**Table 2**

XPS results: surface atomic ratios of the Ni, Mo and Mg in the calcined then in situ reduced samples and the reduction degree of Ni and Mo.

parameter	MoNi0.4 calc	MoNi0.4 red	MoNi0.4_RT calc	MoNi0.4_RT red	Ni calc	Ni red	Mo calc	Mo red	MoNi1.2 calc	MoNi1.2 red
Ni/Mo	6.1	4.5	4.2	2.2	-	-	-	-	0.6	0.6
Mo/Ni	0.16	0.22	0.24	0.45	-	-	-	-	1.67	1.67
Mg/Ni	4.6	7.7	9.8	24.1	9.3	18.9	-	-	13.7	18.4
Mg/Mo	27.7	35	41.6	53.6	-	-	9.4	9.9	7.8	10.5
reduction degree, Ni		100%Ni <sup>0</sup>		100%Ni <sup>0</sup>		40%Ni <sup>0</sup> 60%Ni <sup>2+</sup>				80%Ni <sup>0</sup> 20%Ni <sup>2+</sup>
reduction degree, Mo		63%Mo <sup>0</sup> 22%Mo <sup>4+</sup> 15%Mo <sup>6+</sup>		55%Mo <sup>0</sup> 30%Mo <sup>4+</sup> 15%Mo <sup>6+</sup>				79%Mo <sup>0</sup> 21%Mo <sup>4+</sup>		72%Mo <sup>0</sup> 21%Mo <sup>4+</sup> 7%Mo <sup>6+</sup>

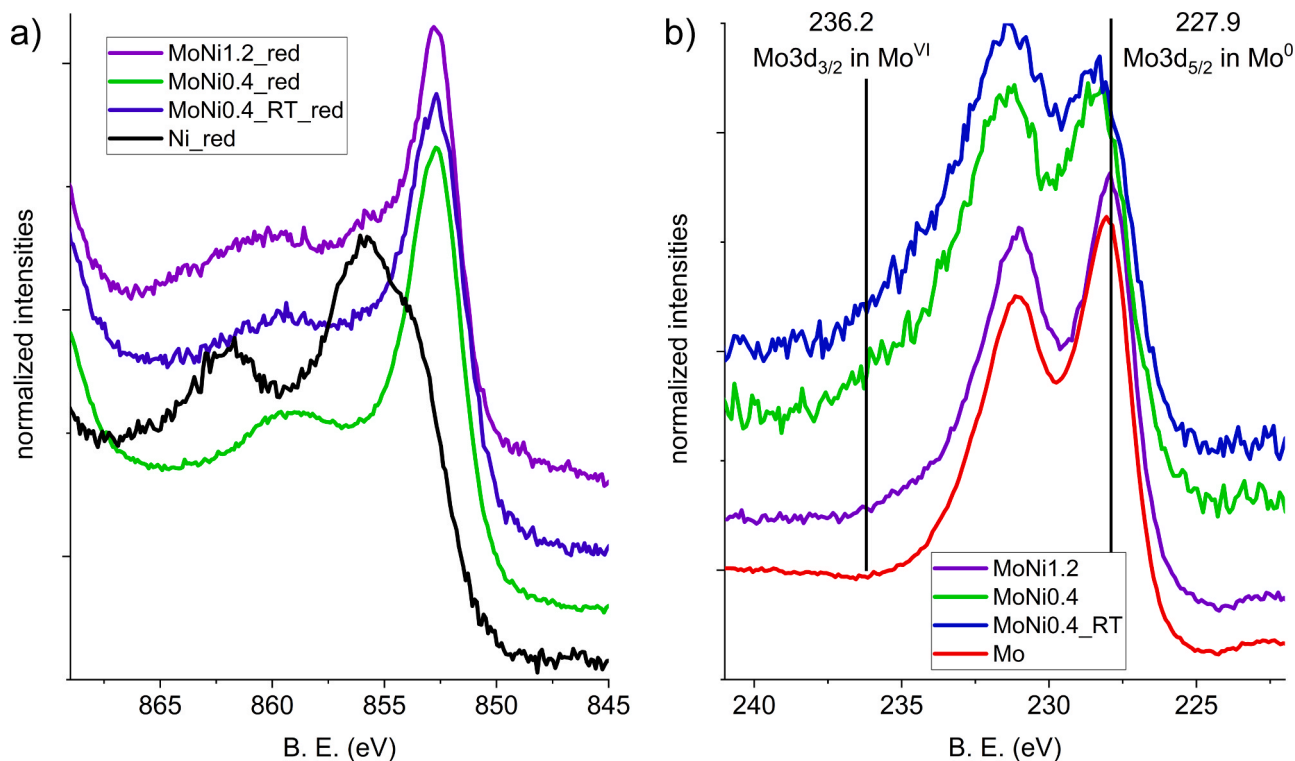


Fig. 6. XPS spectra of the samples after the in situ reduction treatment: (a) Ni 2 p region; (b) Mo 3 d region.

and Mo, respectively), and the bimetallic sample has a 20%  $\text{Ni}^{2+}$  fraction beside metallic Ni. Note, that reduction treatment for MoNi1.2 causes exactly the same change in Mg/Ni and Mg/Mo ratio, and so Mo/Ni value remains the same as in the calcined state. The findings indicate that the surface  $\text{NiMoO}_4$ , which was initially well-dispersed and detected via Raman spectroscopy, underwent a reduction process leading to the creation of an alloy with a Ni/Mo ratio close to 1. This was confirmed through STEM-EDS analysis of the smaller particles. The remaining oxidic components must be anchoring  $\text{Ni}^{2+}$  and Mo(VI), Mo(IV) species around these alloyed particles. The reference Mo sample had very similar Mg/Mo ratio as MoNi1.2, and after reduction the ratio was almost unchanged. This proves the very strong interaction of  $\text{MoO}_x$  and MgO already experienced and resulting in 20% unreduced Mo(IV) amount. XPS measurements showed us that there is a surface enrichment in Mo relative to the bulk Mo/Ni ratio for MoNi1.2 and to a lesser extent for MoNi0.4\_RT, but a depletion in surface Mo for MoNi0.4. This will play a role in catalytic behavior (see below).

### 3.3. Temperature ramped $\text{CH}_4$ decomposition experiments with 1% $\text{CH}_4/\text{He}$

Strongly diluted methane was applied to follow the pyrolysis process with QMS analysis in a Micromeritics AutoChem 2920 instrument. The system allows the detection of fast changes in gas phase within seconds during the course of reaction. These kinds of investigations are very rare in pyrolysis studies, only a few works can be found on Ni-based catalysts that report temperature ramped or isothermal  $\text{CH}_4$  decomposition experiments with QMS analysis. For example, Fierro et al. studying Ni supported on mixed oxides derived from Mg/Al-hydrotalcites [5] or on commercial supports [6] ( $\text{Al}_2\text{O}_3$ , MgO and  $\text{MgO-Al}_2\text{O}_3$ ) experienced a progressive deactivation of Ni catalysts (depending on the reaction conditions and catalyst type) and the formation of defective carbon nanofibers. Fig. 7 depicts our results of the temperature ramped experiments. During our ramped experiments, the catalyst after the in situ reduction pretreatment (800 °C/1 h) was contacted with the methane stream at around 200 °C and heated up to 800 °C then cooled down in

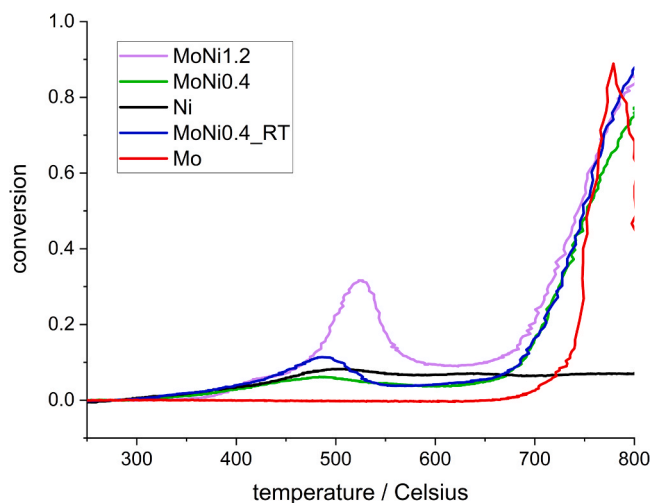


Fig. 7.  $\text{CH}_4$  conversion curves in 1%  $\text{CH}_4/\text{He}$  flow under temperature ramped mode (Conditions: 20 mg catalyst, 30 mL/min flow rate, 10 °C/min).

inert Ar gas. Fig. 7 shows that the pure Mo sample started the methane dissociation only above 670 °C, while Ni catalyst already at 300 °C. The reference Mo catalyst produced a rather unusual abrupt conversion curve reaching its maximum already at 780 °C and a steep fall afterwards, suggesting an extremely fast activation/deactivation process.

The bimetallic samples were active at both the low and the high temperature ranges, and so they behaved as a combination of Ni and Mo. In the low temperature range, MoNi1.2 exhibited the highest activity with a slightly shifted peak maximum. The second most active sample was MoNi0.4\_RT and the least active one was MoNi0.4. The catalytic sites dissociating methane were eventually deactivated (that is why the peak-like shape) at around 550 °C, but there were still active sites in all Ni-containing samples producing a moderate activity in the medium



temperature region. Then, at  $T > 650$  °C, MoNi0.4 and MoNi0.4\_RT first followed exactly the same rise but at the highest temperature MoNi0.4 was left behind and the same catalysts that were the most active in the low temperature range achieved the highest conversion (MoNi1.2 and MoNi0.4\_RT). This result suggests us that there are highly active sites that easily deactivate and others, less active, probably contributing to catalyst longevity. The important thing is that these NiMo surface sites get activated at similar temperature range: the ones that are “Ni-like” surface can dissociate methane easily but deactivate fast, the ones that are alloyed with Mo have active sites working finer and longer but depending on the surface Mo/Ni ratio. This principally reflects the synergy of Mo and Ni.

### 3.4. $\text{CH}_4$ pyrolysis with 50% $\text{CH}_4/\text{Ar}$ and the related XRD, HRTEM, STEM-EDS and Raman structural results

Severe conditions at 800 °C with high methane content were set in the pyrolysis tests carried out in a horizontal reactor. In this arrangement, to provide space for the coke growing process, the gas stream passes above the sample in the quartz tube, therefore, these tests cannot be evaluated as real kinetic measurements and directly compared to the studies in the above fixed bed reactor in AutoChem 2920. Moreover, we did not use additional  $\text{H}_2$ , because the samples were prereduced before the addition of methane. Be aware that the absence of  $\text{H}_2$  co-reactant (rare in the literature) may induce a faster deactivation in our case, since hydrogen addition is able to reduce the amount of amorphous carbon that was thought to be also responsible for deactivation [42].

The pyrolysis tests were planned to last for 3 hours, but in most cases they were stopped earlier (TOS are different, see Table 3), when samples deactivated and no further  $\text{H}_2$  formation was observed. (We did not intend to influence the deposited coke structure simply by a thermal treatment after the loss of activity.) According to Fig. 8, all bimetallic samples started with an initial  $\text{CH}_4$  conversion between 10% and 15%, while the monometallic ones hardly reached 2–4% and deactivated fast. This conversion values may seem low, but it is due to the deliberately low Ni content we set during preparation. On all the bimetallic catalysts the initial  $\text{CH}_4$  dissociation rate significantly slowed after 20 min, but the outstanding catalytic stability of MoNi1.2 sample was apparent. Generally, the activity and stability of the samples resembled the results with the 1%  $\text{CH}_4$  flow experiments. The amount of deposited carbon was determined from the  $\text{CH}_4$  conversion data and nicely correlated with the weighed carbon amount (Table 3). It is apparent that the 3 times higher Mo content increased the so-called carbon yield at least 4 times. The final coke amount reflects well the coke deposition rate (and the methane conversion) in the order of MoNi1.2>MoNi0.4\_RT>MoNi0.4>Mo≈Ni.

The spent samples were characterized by XRD and the diffractograms are shown in Fig. S8. Clue of graphitic carbon at around  $2\theta = 26.5^\circ$  value could be discerned for the bimetallic samples. The wide peak shifted to lower  $2\theta$  values, because the deposited carbon is not a perfect crystalline graphite structure but an irregular, turbostratic graphite constituting the nanotube walls with different wall thicknesses. In samples with Mo/Ni=0.4, some Ni peak was also detectable and the precise

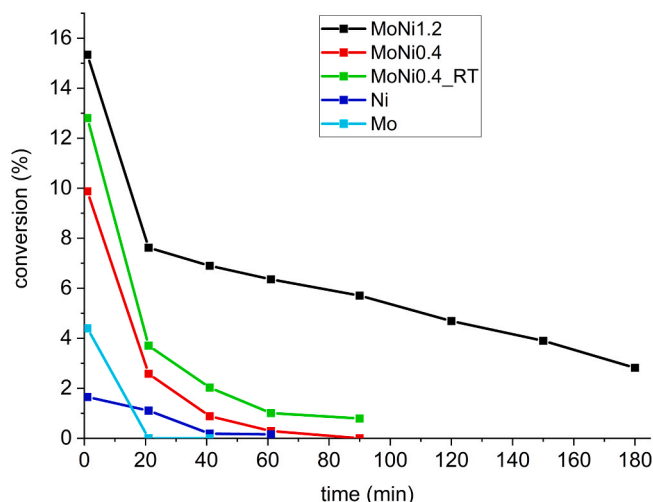


Fig. 8. Methane conversion curves during pyrolysis tests. (Conditions: 50 mg catalyst, 50% $\text{CH}_4/\text{Ar}$ , 60 mL/min,  $T=800$  °C).

fitting gave the same 9% Mo content in nickel for both samples with 8.2 nm crystallite size for MoNi0.4 and 6.3 nm for MoNi0.4\_RT. For MoNi1.2, beside the wide graphite peak, only a hint of  $\text{Mo}_2\text{C}$  peak could be suggested but nothing at the Ni position.

TEM measurements delivered additional information about the morphology and composition of the spent samples. The average metal particle size of the spent samples is collected in Table 1. It is seen, there is no sintering phenomena as usually after high temperature applications, but rather shrinking of particle sizes in agreement with the XRD results above. The bimetallic samples possess larger average particle size than the monometallic ones (as in freshly reduced state), and the sample prepared at room temperature had the largest 8.1 nm average particle size and widest size distribution (as in freshly reduced state). Fig. S9a shows a general TEM image of spent Ni sample with a sole 3.6 nm wide double walled carbon nanotube and nicely distributed Ni particles. The HRTEM image in Fig. S9b proves the carbon deposition around Ni particles in the form of a 0–2 nm thick graphene/graphite layers (signed with arrows). This carbon coverage caused complete deactivation within the first 40 min of the reaction.

As for the Mo sample the view is similar: a lot of dark colored particles were densely distributed on the MgO support (Fig. S10a). If we compare the image with that of the freshly reduced sample (Fig. 3), it seems that more Mo particles are spread on the support after the reaction. That is, the unreduced  $\text{MoO}_2\text{-MoO}_x$  was converted into Mo carbide as the HRTEM images in Figs. S10b–c show: line spacings of 0.227 nm corresponding to  $\text{Mo}_2\text{C}(101)$  and 0.235–0.238 nm corresponding to  $\text{Mo}_2\text{C}(002)$  facets were measured. Around those  $\text{Mo}_2\text{C}$  particles, a 1–5 layer thick rather defective shell of carbon was observed. Remember, this catalyst also deactivated very early during the methane pyrolysis test.

Different picture with several thin and thicker MWCNTs and elongated metal particles occluded inside the tubes or positioned at their ends were obtained for all the bimetallic samples. Fig. 9a reveals the morphology of the spent MoNi0.4 sample. Several carbon nanotubes (width between 5 and 20 nm) of different wall thickness and some amorphous carbon could be observed with metal particles inside or outside of the tubes. The HRTEM image in Fig. 9b shows a 8 nm thick nanotube with 12 sheets of curved graphitic wall (0.34 nm line spacings) covered by an amorphous carbon layer. Fig. 9c and d show a STEM-EDS map and the corresponding HAADF image differentiating the Mo, Ni and Mg containing areas. It is very interesting that there were round-shaped and elongated particles, and their composition was either Mo-rich or Ni-rich. As for the larger (~20 nm), round or pear shaped particles, we could observe significant Ni excess (Mo/Ni~0.07–0.09), while the areas

Table 3

The amount of carbon produced in methane pyrolysis using 50% $\text{CH}_4/\text{Ar}$  flow at 800 °C during the presented time on streams (TOS).

Sample	TOS (min)	C formed as calculated from $\text{CH}_4$ conversion/weighed after the reaction ( $\text{mg}_{\text{carbon}}/50 \text{ mg}_{\text{cat}}$ )	carbon yield=[carbon weight/catalyst weight]*100 (%)
Ni	60	7/0	14
Mo	40	6/0	12
MoNi0.4	90	26/15	52
MoNi0.4_RT	90	42/30	84
MoNi1.2	180	160/160	320

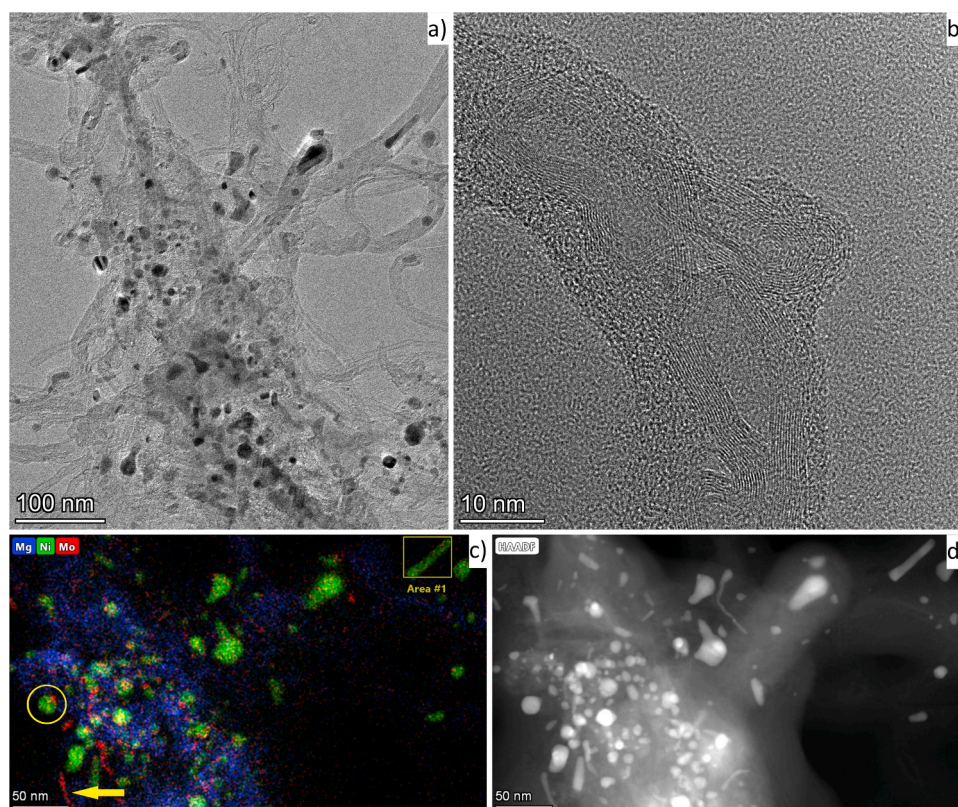


**Fig. 9.** Representative images of the spent MoNi<sub>0.4</sub> catalyst: (a) TEM image of metal particles inside or outside of differently sized carbon nanotubes; (b) HRTEM image of a 8 nm thick nanotube with 12 sheets of curved graphitic wall covered by an amorphous carbon layer; (c) STEM-EDS elemental maps of Mg, Ni and Mo where the framed (Area #1), elongated particle is (unusually) Ni-rich and the circled segregated alloy particle coexist with a separated Mo-rich ductile particle signed with yellow arrow; (d) HAADF image of the same area.

with smaller particles resulted Mo/Ni=0.2 ratio keeping the round shape. The long, thin species were mainly Mo-rich with some exception such as the framed one at the top right corner with Mo/Ni=0.09 value (Area #1). The map shows a definite Mo-Ni segregation process starting with Mo to move to one side of the alloyed particles (circled with yellow) then producing a Mo-rich separate particle seemingly more ductile (marked with a yellow arrow).

This process happens during carbon deposition and dissolution into the alloy particles. The composition detected by XRD corresponds well to the larger sized Ni-rich particles but could not prove the existence of the more disperse Mo-rich species. It was hard to find any sign of such segregation detected by TEM in the literature [19].

Our other low Mo-loaded catalyst showed very similar morphology, except for the absence of amorphous carbon coverage of nanotubes as seen in Fig. 10a-b. Straight or bamboo type carbon nanotubes with 10–20 nm in diameter and 2–5 nm wall thickness were detected. Some onion-type empty structures were also observed (Fig. 10b). This morphology could be formed by the influence of Mo<sub>2</sub>C of around 1 nm size as suggested in the literature [43].

The alloy segregation was also observable in long particles as shown in the TEM image and the STEM-EDS maps in Fig. 10c-d of MoNi<sub>0.4</sub> RT. There is a smooth transition between the Ni-rich head (Mo/Ni=0.09) and the Mo-rich tail (Mo/Ni=1.5) in the circled part of the image (golf-stick shaped particle). The uneven distribution of Mo in the small particle signed with the rectangle is also evident.

The best catalyst sample in terms of activity and stability under all conditions was MoNi<sub>1.2</sub> shown in Fig. 11a-f. Very long, sometimes more than 2  $\mu$ m carbon nanotubes could be detected with about 5–10 nm in diameter. Catalyst particles (support and metal) were dispersed within the clumps of MWCNTs, and the average metal particle size was 6.3  $\pm$  3.5 nm (see Fig. 11a-b). Those particles were either inside the tubes or

at their ends, some of them completely elongated. The thinnest tubes consisted of 1.8 nm thick wall made of 5 layers of graphene, and the inner diameter was only 2.6 nm (Fig. S11). As for the Mo and Ni distribution, Fig. 11c and d show that particles of about 5–8 nm closely grouped to each other result Mo/Ni=0.9 that is just the same as the starting value before the reaction. The smaller particles inside the tubes or attached on their surface were hard to quantify because of the large error at such a low EDS count values. However, according to Fig. 11e-f, most of them contains Mo and Ni as well. It seems alloy segregation in this sample was not so profound or we could not detect many larger, Ni rich particles as before (XRD gave only noticeable peak of such Ni-rich alloyed crystallites). One extra observation in this sample was the detection of intimate contact of carbon nanotubes with tiny Mo-containing MgO patches as it is seen in Fig. 11f. This shows that metallic (Ni)Mo particles were in strong interaction with the restructured MgO support beneath. Remember, in the calcined sample MgO restructuring was observed by XRD because of the occlusion of Mo-oxides. This MgO after the disclosure of small reduced (Ni)Mo particles stayed around and could even moderate the nanotube growth by its basicity.

Finally, the Raman spectroscopy results will be analyzed, as this is a common approach in pyrolysis studies for assessing the nature of deposited carbon. In such studies, the focus often revolves around the ratio of two primary Raman bands. The first is the G-band, which serves as a prominent indicator of carbon crystallinity, while the second is the D-band, referred to as the disorder band, which becomes active when an sp<sup>2</sup> carbon ring is adjacent to a graphene edge or a defect. The I<sub>D</sub>/I<sub>G</sub> intensity ratio, which quantifies the ratio of the integrated area of these two bands, is a widely adopted metric for characterizing the extent of defects in MWCNTs and various graphitic materials [19,25,26]. Raman spectra of the catalysts with the carbon product after the CH<sub>4</sub>



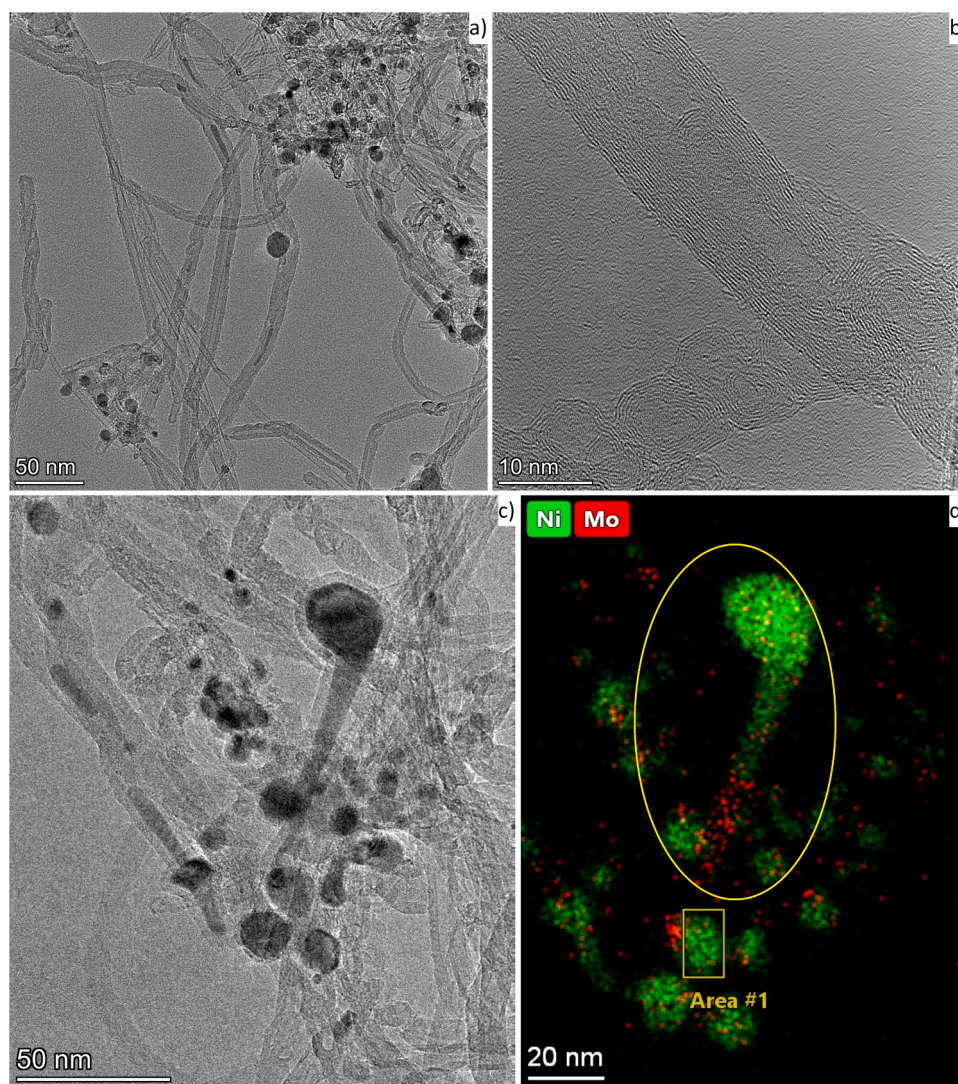


**Fig. 10.** Representative images of the spent MoNi<sub>0.4</sub> RT catalyst: (a) TEM image of metal particles inside or outside of carbon nanotubes of 10–20 nm; (b) HRTEM image of a 10 nm thick nanotubes and unique empty nanoonions; (c) TEM image of a catalyst area with a segregating NiMo golf-stick shaped alloy particle covered by carbon; (d) TEM-EDS elemental maps of Ni and Mo of the same area, the head of the circled golf-stick is Ni-rich, the tail is Mo-rich and the other framed Area #1 shows another metal segregation process started within a single particle.

decomposition at 800 °C are presented in Fig. 12. The bands in the first order Raman region of carbon could be well fitted with the following four bands: 1) the G band between 1570 and 1597  $\text{cm}^{-1}$  belonging to the in-plane stretching mode of the  $\text{sp}^2$  C-C bonds and the three defect-activated D bands such as 2) the D “breathing mode” from  $\text{sp}^2$  carbon rings between 1326 and 1346  $\text{cm}^{-1}$ ; 3) the D2 band [44] around 1607–1610  $\text{cm}^{-1}$  and 4) the D3 band in the range of 1495–1538  $\text{cm}^{-1}$  assigned to amorphous carbon with different  $\text{sp}^3$  content [45]. In the second Raman region the 2D band serves as an indicator of the presence of long-range order in the material [46] (overtone of breathing mode of hexagonal rings) and between 2641 and 2664  $\text{cm}^{-1}$  it was visible for most of the samples, and in some cases, also a weak D+D2 combination band around 2950  $\text{cm}^{-1}$  could be found. The peak at  $\sim 2330 \text{ cm}^{-1}$  is due to the Raman mode of  $\text{N}_2$  gas in air. The sharp peak at 1556  $\text{cm}^{-1}$  in the spectra of both Ni and Mo samples does not belong to the carbon product, but rather to a modified MgO species, because it appeared also for calcined and reduced Mo sample, but not for pure MgO and was observed by others as well [47]. The most important parameters of these fitted bands are collected in Table 4.

The spectra of the monometallic samples in Fig. 12 significantly differs from those of the bimetallic ones and from each other as well.

This shows that the structure of the limited amount of carbon generated by these catalysts before their rapid deactivation is notably distinct. The Raman spectrum of the Ni sample has the narrowest G-band at 1580  $\text{cm}^{-1}$  and only a small D-band at 1336  $\text{cm}^{-1}$ , resulting in the lowest  $I_D/I_G$  ratio. These features can be assigned to a few layers of graphene [44] or a turbostratic graphite [48] in accordance with the TEM and XRD findings. Besides, presence of amorphous carbon is also suggested by D3 band centered at 1538  $\text{cm}^{-1}$  in the highest relative amount ( $I_{D3}/I_G=1.1$ ) among all catalysts. In case of the Mo sample, the large FWHM of G band, the highest  $I_D/I_G$  value and the missing 2D band indicates low three-dimensional ordering. Generally, the FWHM of G-band always increases with disorder [49]. The spectra of Mo catalyst can be assigned to transition to nanocrystalline graphite [50] or rather to carbon black [51]. It is interesting that when nanotubes were reported to form over Mo/MgO catalysts, the resulting  $I_D/I_G$  ratios were also higher than unity [9,11]. (It's important to emphasize that we did not observe any carbon nanotubes in our sample. Instead, what we identified were short-range ordered graphene-like, partial shells enveloping Mo-carbide particles, characterized by an  $I_D/I_G$  ratio of 2.24.) It is known that carbon black primary particles consist of concentrically arranged graphitic-like domains that are made up by polyaromatic layers



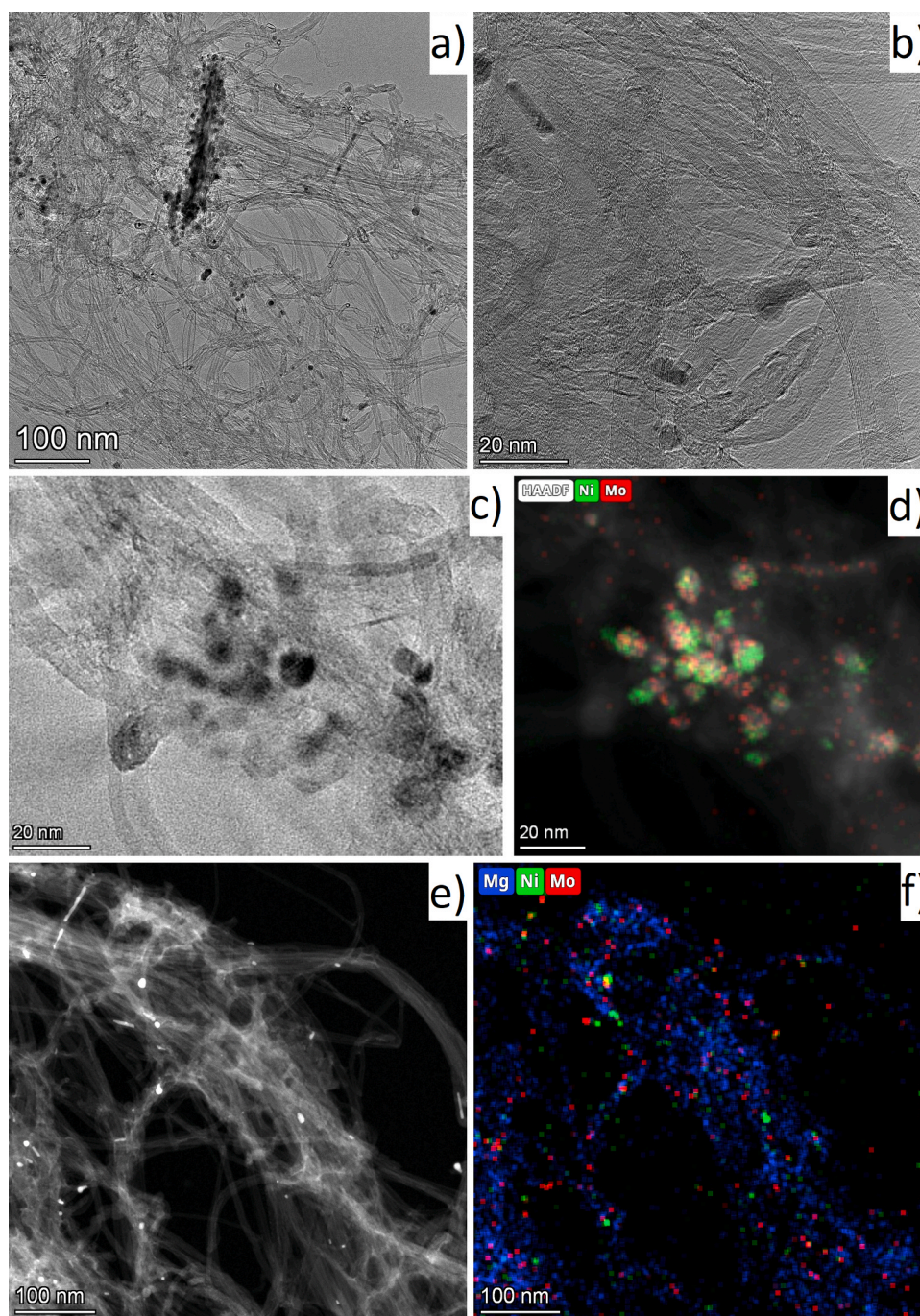


**Fig. 11.** Representative images of the spent MoNi1.2 catalyst: (a) TEM image of nanotube clumps with catalyst moieties; (b) HRTEM image with metal particles at the end or inside of the thin carbon nanotubes; (c) TEM image of a distinct area with several metal particles of 5–8 nm; (d) the TEM-EDS elemental map of Ni and Mo and the HAADF image of the same area resulting Mo/Ni=0.9; (e) HAADF image of thin carbon nanotubes and the occluded metal particles; (f) the TEM-EDS elemental map of Mg, Ni and Mo of the same area suggesting that the carbon nanotubes are coupled with tiny Mo-containing MgO patches.

[51]. This polyaromatic layers – beside short graphene patches – were probably formed in our pure Mo sample as this is the intrinsic property of molybdenum(oxide) when contacting  $\text{CH}_4$  (high selectivity to ethylene that can polymerize) as discussed in refs [12,52].

The bimetallic samples have spectra similar to each other with respect of the G and D band positions and the FWHM values. The position of G bands reflects that instead of graphitic carbon shells, carbon nanotubes were formed. The  $I_D/I_G$  ratios are all higher than that of the Ni sample. MoNi0.4 with the lowest  $I_D/I_G = 0.28$ , the lower frequency 2D band and the largest relative intensity of D3 band (contribution from amorphous carbon) falls closest to our Ni sample. Thus, we can deduce

that carbon formed on MoNi0.4 is more similar to that on Ni, the carbon nanotubes are less defective but the proportion of amorphous carbon is higher than in carbon products in the other bimetallic catalysts. These other two samples were better catalysts in pyrolysis tests – or otherwise, the MoNi0.4 sample having more perfect nanotubes deactivated the most. The best MoNi1.2 catalyst produced the least amorphous carbon and the most, moderately defective MWCNTs.



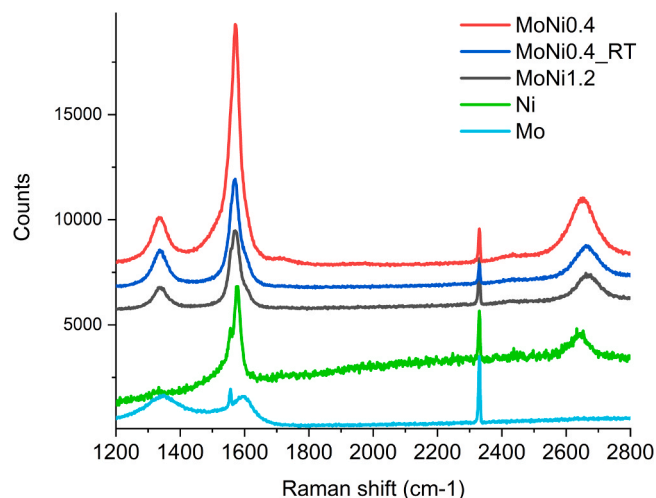


**Fig. 12.** The Raman spectra of the spent catalysts after methane pyrolysis test at 800 °C with the characteristic carbon bands. (The fitting results are provided in Table 4.).

### 3.5. The dynamic interaction of nickel and molybdenum leading to synergism in pyrolysis

Based on all structural and catalytic results reported in this work, we can deliver a picture of the synergistic effect observed in our Mo-Ni catalysts up to the Mo/Ni=1 ratio. It is important to note that particle size range for all of our samples was between 5 and 8 nm. This means that particle size difference could not be the cause of the differences observed in the catalytic behavior of the samples.

Neither the monometallic Mo, nor the Ni sample could produce notable carbon product and H<sub>2</sub> gas under the conditions applied, while the best combination of the 2 metals could deliver 320% carbon yield. CH<sub>4</sub> dissociation is much harder on metallic molybdenum than on nickel and requires high temperature. The activity of Mo-carbide in CH<sub>4</sub> dissociation depends on the carbon content of Mo: carbon-deficient Mo nanoparticles are very reactive, but they feature low stability due to the strong binding of the adsorbed CH<sub>x</sub> species (site blocking effect by CH<sub>x</sub>) [53]. This could be the reason of extreme fast increase of CH<sub>4</sub> decomposition then abrupt decrease of activity of our Mo catalyst sample. Although there is a high metal dispersion in Mo sample, the small particles got easily covered with a partial shell of graphene layers and amorphous carbon species (CH<sub>x</sub>) without the burst of nanotube growth at 800 °C.

The other reference point is the similar sized (d=5 nm) nickel particle over MgO. In this case CH<sub>4</sub> dissociation did not require so high temperature as for Mo, but again, under our conditions nice graphitic layers covered the metal particles and only very few, thin MWNTs were formed before the catalyst finished working. This is in accordance with the literature, namely, encapsulating type, more graphitic carbon was detected on the easily deactivating Ni catalyst [6] (and less ordered MWNTs were formed on the less deactivating samples). Thus, it seems that the oriented carbon diffusion within or around the surface of Ni particles to build nanotubes was slow or actually absent, but the CH<sub>4</sub>

dissociation step on the surface atoms was fast. In connection with the fast deactivation we have to mention that Ni sample with the smallest average particle size contained the most amorphous carbon (Raman results) that is also a characteristics of fast deactivation in the absence of hydrogen co-reactant during pyrolysis [42].

For the efficient and continuous nanotube growth, the CH<sub>4</sub> dissociation and the carbon diffusion, precipitation, then the growth of graphene layers, their orientation into tube morphology should be well in equilibrium. It was already declared in the literature that Ni is responsible for the dissociation of CH<sub>4</sub> into carbon and Mo<sub>2</sub>C works as a carbon reservoir [24,26,27]. To this simple picture we can add the followings. When Ni and Mo atoms are present side by side on the particle surface, the originally fast dissociation step is slowed down, because the number of Ni atoms is less and/or because they are electronically influenced by Mo atoms. We noticed that the intensity and the temperature of the first CH<sub>4</sub> decomposition peak during the methane decomposition ramped reaction are in line with the catalytic activity under harsher conditions in the pyrolysis reactor – and this reflects the different CH<sub>4</sub> dissociation ability of different alloy particles. On the other side, it seems, the carbon diffusion step is promoted by Mo that acts as a “carbon extractor” and let the Ni sites dissociate another CH<sub>4</sub> molecules again. This is exhibited as a synergistic effect resulting the growth of nanotubes when it is observed neither on Mo nor on Ni samples.

First, we should distinguish between cases i) when the number of Ni atoms is predominant over that of Mo atoms or ii) they are about the same. As for the low Mo-loaded samples, Ni is the main metal component that would be expected to determine the catalytic properties. Under the same Mo/Ni ratio (Mo/Ni=0.4) with very similar metal loadings, however, the surface Mo and Ni concentrations are different (XPS results, Table 2) and it appears that the surface Mo/Ni ratio is the governing parameter in the catalytic reaction. Although bimetallic particles with higher Mo content are present in MoNi0.4 (STEM-EDS, XRD results), the catalyst surface is enriched in nickel (Mo/Ni by XPS is less) and this is not beneficial. While the opposite is true on MoNi0.4\_RT: when the bimetallic particles are poorer in molybdenum (STEM-EDS, XRD results), but the MoO<sub>x</sub> dispersed in the very top layer of the support and/or Mo on the surface of bimetallic particles determine the catalytic property leading to a more stable catalytic activity and a more efficient carbon nanotube formation. Moreover, the surface Mo excess seems to be more important than the particle size and size distribution in respect of catalyst longevity, this is why MoNi0.4\_RT works longer than MoNi0.4.

When the atomic ratio of Mo and Ni is about the same, the situation is different. The synthesis process successfully produced small d<5 nm bimetallic particles with about 1:1=Ni:Mo ratio upon the reduction of the two oxidic components that were in close contact within the pores of the MgO matrix. The so-called larger Ni-rich particles were under 10 nm here with much more Mo content than in the MoNi0.4 samples. In the case of the small particles, alloy segregation during the reaction was not observed as the same composition was detected after the pyrolysis as before (Mo/Ni~0.9). These NiMo particles were anchored by the remaining MoO<sub>x</sub>-NiO<sub>x</sub> moieties in the top layer of MgO. This might contribute to the less segregation and the higher dispersion as well. We can thus deduce that an alloy with above 30% Mo is more stable during pyrolysis (segregation is less pronounced), while the 1:1 alloy is a far

**Table 4**

Raman results of the characteristic carbon bands detected over the catalysts after pyrolysis at T=800 °C.

Sample	G (cm <sup>-1</sup> )	FWHM <sub>G</sub> (cm <sup>-1</sup> )	D (cm <sup>-1</sup> )	D2 (cm <sup>-1</sup> )	D3 (cm <sup>-1</sup> )	2D (cm <sup>-1</sup> )	I <sub>D</sub> /I <sub>G</sub>	I <sub>D3</sub> /I <sub>G</sub>
MoNi1.2	1571	40	1339	1608	1539	2667	0.51	0.08
MoNi0.4	1570	35	1336	1609	1534	2649	0.28	0.42
MoNi0.4_RT	1570	34	1337	1606	1508	2662	0.60	0.21
Ni	1580	20	1336	-	1538	2641	0.13	1.12
Mo	1597	72	1344	-	1515	-	2.24	0.84

better composition to provide equilibrium between the CH<sub>4</sub> activation and carbon transport leading to high yield of nanotubes. This ~1:1 alloy with high dispersion was not present in the other two bimetallic catalysts; this is why the catalytic activity differed so much. (Remember, the end conversion of CH<sub>4</sub> during pyrolysis at 800 °C was still 3% and not zero over the MoNi<sub>1.2</sub> sample.)

The most significant novelty of our work is the exploration of the composition-dependent nanoscale segregation of bimetallic particles during carbon deposition process. In the Ni-rich larger particles because of the carbon diffusion, Mo segregates inside, then with the creation of nanotubes it forms separated Mo-rich particle and the original entity becomes even more Ni-rich but with smaller size. Similar phenomenon, the so-called self-dispersion was observed in the case of bulk NiSn alloys upon ethylene contact. This assumed to happen via the formation of a second carbon containing alloy creating intergranular boundaries in the volume of the alloy, along which the alloy actively dispersed [42]. Furthermore, rapid disintegration of the bulk NiCu and NiMo alloy catalysts during contact with the hydrocarbon reaction mixture was observed and explained with the formation of active particles catalyzing the growth of carbon filaments [54,55]. The question is open if the metallic alloy or carbide phase is the active entity during the reaction if we start out from reduced catalyst. The existence of crystalline ternary Ni<sub>x</sub>Mo<sub>y</sub>C<sub>z</sub> carbides was shown by XRD when bulk MoNi alloy particles with only 6% SiO<sub>2</sub> content were produced by a Pechini-based method [41]. Thus, we can suppose (but not prove) that a ternary Ni<sub>x</sub>Mo<sub>y</sub>C<sub>z</sub> carbide forms in our case as well at the start of the reaction and the contribution from the different alloy carbides determines the apparent pyrolytic activity and stability. In the case of MoNi<sub>1.2</sub>, as metal particles with equimolar Ni-Mo composition are numerous, one may suggest that a MoNiC<sub>2</sub> carbide is the main active entity of the reaction here and it provides the least segregation and the best carbon formation rate under our conditions.

#### 4. Conclusions

For methane catalytic decomposition in inert atmosphere, different NiMo/MgO catalysts were produced and investigated here. Synergetic interaction between nickel and molybdenum was declared in the literature for a wide range of metal concentrations. Our aim was to reveal the reasons of such synergism in the case when the active metal components are below the 10 nm size range. In our work, simultaneous deposition of metal precursor ions was done in aqueous phase based on the adsorption sites of MgO support. The theoretical 7 wt% nickel content was obtainable, while molybdenate loading was limited but could be increased to 13 wt% by the increase of the synthesis temperature. Shortly, two bimetallic catalysts with Mo/Ni=0.4 ratio were obtained at room temperature and at 80 °C, and one with Mo/Ni=1.2 ratio at 80 °C. Reference Mo/MgO and Ni/MgO catalysts were prepared at 80 °C via the same adsorption-precipitation method.

TPR measurements ascertained the complete reduction of Mo(VI) and Ni(II) up to 800 °C in the bimetallic samples, but the monometallic samples still contained some oxidic MoO<sub>x</sub> or NiO<sub>x</sub> components. This means the reducibility was increased in the bimetallic samples. Average particle size of the reduced samples was below 8 nm in all cases, and STEM-EDS analysis showed that the larger alloy particles mostly seen in samples with Mo/Ni=0.4 ratio were all extremely Ni-rich, while the smaller contained more Mo. This was in perfect agreement with the XRD results. The catalyst with Mo/Ni=1.2 ratio contained XRD-silent smaller nanoparticles, but according to the STEM-EDS, with a maximum 1/1 ratio of the two metals and some separated Mo entities in the MgO support. In situ XPS carried out on reduced samples showed a surface Mo excess (compared to the bulk Mo/Ni ratio) for sample with Mo/Ni=1.2 ratio and for the bimetallic catalyst with lower Mo loading prepared at 25 °C. The catalytic methane decomposition experiments carried out either in highly diluted CH<sub>4</sub> flow in temperature ramped mode or with a 50% CH<sub>4</sub>/Ar stream at 800 °C showed the existence of synergism for the

bimetallic samples. These catalysts produced moderately irregular graphitic MWNTs with different yields. The monometallic Ni and Mo in turn deactivated quickly after forming only several layers of well-ordered graphene around Ni or not complete, highly defective carbon shells around Mo particles (basically encapsulating type carbons) and also some amorphous carbon, in much larger proportion than on bimetallic samples. The superiority of the catalyst with Mo/Ni=1.2 ratio in terms of activity, stability and carbon yield was explained by the stability of the equimolar alloyed NiMo particles that did not seem to segregate during the carbon nanotube growth process unlike the ones in the other catalysts with Mo/Ni=0.4 ratio.

Our results will hopefully help to clarify the interaction of catalyst structure and performance that greatly influences the amount of H<sub>2</sub> and the purity and morphology of carbon products, and contribute to make a step forward in catalytic methane pyrolysis with the tools of basic research.

#### CRedit authorship contribution statement

**Tamás I. Korányi:** Writing – review & editing, Supervision. **Zoltán May:** Investigation. **István Rigó:** Visualization, Investigation. **Zsolt Endre Horváth:** Visualization, Investigation. **György Sáfrán:** Methodology, Investigation. **Andrea Beck:** Writing – review & editing, Methodology, Investigation. **Miklós Németh:** Writing – original draft, Visualization, Methodology, Investigation. **Anita Horváth:** Writing – review & editing, Writing – original draft, Methodology, Investigation, Funding acquisition, Conceptualization.

#### Declaration of Competing Interest

The authors declare that they have no known competing financial interests or personal relationships that could have appeared to influence the work reported in this paper.

#### Data availability

Data will be made available on request.

#### Acknowledgements

We thank the Centre for Energy Research, The Hungarian Academy of Sciences (bilateral HAS-CNR #NKM2023-14) and the Hungarian Scientific Research Fund (OTKA K143216 and K146032) for the financial support. The authors are grateful to Prof. Miklós Veres for the discussions of Raman results and Prof. Krisztina László for the BET measurements.

#### Appendix A. Supporting information

Supplementary data associated with this article can be found in the online version at [doi:10.1016/j.apcata.2024.119651](https://doi.org/10.1016/j.apcata.2024.119651).

#### References

- [1] W. Yan, S.K. Hoekman, Production of CO<sub>2</sub>-free hydrogen from methane dissociation: a review, *Environ. Prog. Sustain. Energy* 33 (2014) 213–219, <https://doi.org/10.1002/ep.11746>.
- [2] N.Z. Muradov, T.N. Veziroğlu, From hydrocarbon to hydrogen-carbon to hydrogen economy, *Int. J. Hydrog. Energy* 30 (2005) 225–237, <https://doi.org/10.1016/j.ijhydene.2004.03.033>.
- [3] A.L. Dipu, Methane decomposition into CO<sub>x</sub>-free hydrogen over a Ni-based catalyst: an overview, *Int. J. Energy Res.* 45 (2021) 9858–9877, <https://doi.org/10.1002/er.6541>.
- [4] K. Salipira, N.J. Coville, M.S. Scurrall, Carbon produced by the catalytic decomposition of methane on nickel: carbon yields and carbon structure as a function of catalyst properties, *J. Nat. Gas Sci. Eng.* 32 (2016) 501–511, <https://doi.org/10.1016/j.jngse.2016.04.027>.
- [5] C. García-Sancho, R. Guil-López, L. Pascual, P. Maireles-Torres, R.M. Navarro, J.L. G. Fierro, Optimization of nickel loading of mixed oxide catalyst ex -hydrotalcite

- for H<sub>2</sub> production by methane decomposition, *Appl. Catal. A Gen.* 548 (2017) 71–82, <https://doi.org/10.1016/j.apcata.2017.07.038>.
- [6] C. García-Sánchez, R. Guill-López, A. Sebastián-López, R.M. Navarro, J.L.G. Fierro, Hydrogen production by methane decomposition: a comparative study of supported and bulk ex-hydrotalcite mixed oxide catalysts with Ni, Mg and Al, *Int. J. Hydrog. Energy* 43 (2018) 9607–9621, <https://doi.org/10.1016/j.ijhydene.2018.04.021>.
  - [7] K. Otsuka, S. Takenaka, Production of hydrogen from methane by a CO<sub>2</sub> emission-suppressed process: methane decomposition and gasification of carbon nanofibers, *Catal. Surv. Asia* 8 (2004) 77–90, <https://doi.org/10.1023/B:CATS.0000026989.55379.10>.
  - [8] N. Sánchez-Bastardo, R. Schlögl, H. Ruland, Methane pyrolysis for CO<sub>2</sub>-free H<sub>2</sub> production: a green process to overcome renewable energies unsteadiness, *Chem. Ing. Tech.* 92 (2020) 1596–1609, <https://doi.org/10.1002/cite.202000029>.
  - [9] A.E. Awadallah, M.A. Deyab, H.A. Ahmed, Mo/MgO as an efficient catalyst for methane decomposition into COx-free hydrogen and multi-walled carbon nanotubes, *J. Environ. Chem. Eng.* 9 (2021) 106023, <https://doi.org/10.1016/j.jece.2021.106023>.
  - [10] Y. Li, X.B. Zhang, X.Y. Tao, J.M. Xu, F. Chen, L.H. Shen, X.F. Yang, F. Liu, G. V. Tendeloo, H.J. Geise, Single phase MgMoO<sub>4</sub> as catalyst for the synthesis of bundled multi-wall carbon nanotubes by CVD, *Carbon* 43 (2005) 1325–1328, <https://doi.org/10.1016/j.carbon.2004.12.022>.
  - [11] Z. Shang, S. Huang, X. Xu, J. Chen, Mo/MgO from avalanche-like reduction of MgMoO<sub>4</sub> for high efficient growth of multi-walled carbon nanotubes by chemical vapor deposition, *Mater. Chem. Phys.* 114 (2009) 173–178, <https://doi.org/10.1016/j.matchemphys.2008.09.022>.
  - [12] W. Ding, S. Li, G.D. Meitzner, E. Iglesia, Methane conversion to aromatics on Mo/H-ZSM5: structure of molybdenum species in working catalysts, *J. Phys. Chem. B* 105 (2001) 506–513, <https://doi.org/10.1021/jp0030692>.
  - [13] X. Xu, F. Fagloni, W.A. Goddard, Methane activation by transition-metal oxides, MO<sub>x</sub> (M = Cr, Mo, W; x = 1, 2, 3), *J. Phys. Chem. A* 106 (2002) 7171–7176, <https://doi.org/10.1021/jp014572x>.
  - [14] F. Solymosi, J. Cserényi, A. Szőke, T. Bánsági, A. Oszkó, Aromatization of methane over supported and unsupported Mo-based catalysts, *J. Catal.* 165 (1997) 150–161, <https://doi.org/10.1006/jcat.1997.1478>.
  - [15] A.E. Awadallah, A.A. Aboul-Enein, M.A. Azab, Y.K. Abdel-Monem, Influence of Mo or Cu doping in Fe/MgO catalyst for synthesis of single-walled carbon nanotubes by catalytic chemical vapor deposition of methane, *Fuller., Nanotub. Carbon Nanostruct.* 25 (2017) 256–264, <https://doi.org/10.1080/1536383X.2017.1283619>.
  - [16] A.A. Aboul-Enein, A.E. Awadallah, Impact of Co/Mo ratio on the activity of CoMo/MgO catalyst for production of high-quality multi-walled carbon nanotubes from polyethylene waste, *Mater. Chem. Phys.* 238 (2019) 121879, <https://doi.org/10.1016/j.matchemphys.2019.121879>.
  - [17] W.-M. Yeoh, K.-Y. Lee, S.-P. Chai, K.-T. Lee, A.R. Mohamed, Effective synthesis of carbon nanotubes via catalytic decomposition of methane: Influence of calcination temperature on metal-support interaction of Co-Mo/MgO catalyst, *J. Phys. Chem. Solids* 74 (2013) 1553–1559, <https://doi.org/10.1016/j.jpcs.2013.05.023>.
  - [18] A.E. Awadallah, A.A. Aboul-Enein, A.K. Aboul-Gheit, Impact of group VI metals addition to Co/MgO catalyst for non-oxidative decomposition of methane into COx-free hydrogen and carbon nanotubes, *Fuel* 129 (2014) 27–36, <https://doi.org/10.1016/j.fuel.2014.03.038>.
  - [19] E.V. Lobiak, E.V. Shlyakhova, L.G. Bulusheva, P.E. Plyusnin, Yu.V. Shubin, A. V. Okotrub, Ni-Mo and Co-Mo alloy nanoparticles for catalytic chemical vapor deposition synthesis of carbon nanotubes, *J. Alloy. Compd.* 621 (2015) 351–356, <https://doi.org/10.1016/j.jallcom.2014.09.220>.
  - [20] A.E. Awadallah, Promoting effect of group VI metals on Ni/MgO for catalytic growth of carbon nanotubes by ethylene chemical vapour deposition, *Chem. Pap.* 69 (2015) 316–324, <https://doi.org/10.1515/chempap-2015-0029>.
  - [21] G.S. Bajad, S.K. Tiwari, R.P. Vijayakumar, Synthesis and characterization of CNTs using polypropylene waste as precursor, *Mater. Sci. Eng. B* 194 (2015) 68–77, <https://doi.org/10.1016/j.mseb.2015.01.004>.
  - [22] R. Song, Q. Ji, Synthesis of carbon nanotubes from polypropylene in the presence of Ni/Mo/MgO catalysts via combustion, *Chem. Lett.* 40 (2011) 1110–1112, <https://doi.org/10.1246/cl.2011.1110>.
  - [23] H.U. Modekwe, M. Mamo, K. Moothi, M.O. Daramola, Synthesis of bimetallic NiMo/MgO catalyst for catalytic conversion of waste plastics (polypropylene) to carbon nanotubes (CNTs) via chemical vapour deposition method, *Mater. Today Proc.* 38 (2021) 549–552, <https://doi.org/10.1016/j.matpr.2020.02.398>.
  - [24] J.D. Núñez, W.K. Maser, M. Carmen Mayoral, J.M. Andrés, A.M. Benito, Platelet-like catalyst design for high yield production of multi-walled carbon nanotubes by catalytic chemical vapor deposition, *Carbon* 49 (2011) 2483–2491, <https://doi.org/10.1016/j.carbon.2011.02.018>.
  - [25] A.E. Awadallah, A.A. Aboul-Enein, A.K. Aboul-Gheit, Various nickel doping in commercial Ni-Mo/Al<sub>2</sub>O<sub>3</sub> as catalysts for natural gas decomposition to COx-free hydrogen production, *Renew. Energy* 57 (2013) 671–678, <https://doi.org/10.1016/j.renene.2013.02.024>.
  - [26] Y. Li, X.B. Zhang, X.Y. Tao, J.M. Xu, W.Z. Huang, J.H. Luo, Z.Q. Luo, T. Li, F. Liu, Y. Bao, H.J. Geise, Mass production of high-quality multi-walled carbon nanotube bundles on a Ni/Mo/MgO catalyst, *Carbon* 43 (2005) 295–301, <https://doi.org/10.1016/j.carbon.2004.09.014>.
  - [27] L.-P. Zhou, K. Ohta, K. Kuroda, N. Lei, K. Matsuishi, L. Gao, T. Matsumoto, J. Nakamura, Catalytic functions of Mo/Ni/MgO in the synthesis of thin carbon nanotubes, *J. Phys. Chem. B* 109 (2005) 4439–4447, <https://doi.org/10.1021/jp045284e>.
  - [28] S. Subramanian, The temperature dependence of the point of zero charge of  $\gamma$ -Al<sub>2</sub>O<sub>3</sub>, TiO<sub>2</sub>, and physical mixtures, *J. Catal.* 117 (1989) 512–518, [https://doi.org/10.1016/0021-9517\(89\)90360-6](https://doi.org/10.1016/0021-9517(89)90360-6).
  - [29] X. Tang, L. Guo, C. Chen, Q. Liu, T. Li, Y. Zhu, The analysis of magnesium oxide hydration in three-phase reaction system, *J. Solid State Chem.* 213 (2014) 32–37, <https://doi.org/10.1016/j.jssc.2014.01.036>.
  - [30] D. Kim, K. Segawa, T. Soeya, I. Wachs, Surface structures of supported molybdenum oxide catalysts under ambient conditions, *J. Catal.* 136 (1992) 539–553, [https://doi.org/10.1016/0021-9517\(92\)90084-U](https://doi.org/10.1016/0021-9517(92)90084-U).
  - [31] D.S. Kim, Y. Kurusu, I.E. Wachs, F.D. Hardcastle, K. Segawa, Physicochemical properties of MoO<sub>3</sub> TiO<sub>2</sub> prepared by an equilibrium adsorption method, *J. Catal.* 120 (1989) 325–336, [https://doi.org/10.1016/0021-9517\(89\)90273-X](https://doi.org/10.1016/0021-9517(89)90273-X).
  - [32] S.Rs. ijsr V. Manikantan Nair, International Journal of Science and Research (IJSR), Synthesis and Characterization of Nanostructured Mg(OH)<sub>2</sub> and MgO, IJSR, Call for Papers, Online Journal, International Journal of Science and Research (IJSR) (n.d.), (<https://www.ijssr.net/>) (Accessed 8 March 2023) (2023).
  - [33] S.C. Chang, M.A. Leugers, S.R. Bare, Surface chemistry of magnesium oxide-supported molybdenum oxide: an in situ Raman spectroscopic study, *J. Phys. Chem.* 96 (1992) 10358–10365, <https://doi.org/10.1021/j100204a048>.
  - [34] M. Chen, J.-L. Wu, Y.-M. Liu, Y. Cao, L. Guo, H.-Y. He, K.-N. Fan, A practical grinding-assisted dry synthesis of nanocrystalline NiMoO<sub>4</sub> polymorphs for oxidative dehydrogenation of propane, *J. Solid State Chem.* 184 (2011) 3357–3363, <https://doi.org/10.1016/j.jssc.2011.10.024>.
  - [35] A.P. De Moura, L.H. De Oliveira, I.L.V. Rosa, C.S. Xavier, P.N. Lisboa-Filho, M.S. Li, F.A. La Porta, E. Longo, J.A. Varela, Structural, optical, and magnetic properties of NiMoO<sub>4</sub> nanorods prepared by microwave sintering, *Sci. World J.* 2015 (2015) 1–8, <https://doi.org/10.1155/2015/315084>.
  - [36] G. Caravaggio, L. Nossova, M.J. Turnbull, Nickel-magnesium mixed oxide catalyst for low temperature methane oxidation, *Chem. Eng. J.* 405 (2021) 126862, <https://doi.org/10.1016/j.cej.2020.126862>.
  - [37] A. Heidarinassab, M. Soltanieh, M. Ardjmand, H. Ahmadvanahi, M. Bahmani, Comparison of Mo/MgO and Mo/γ-Al<sub>2</sub>O<sub>3</sub> catalysts: impact of support on the structure and dibenzothiophene hydrodesulfurization reaction pathways, *Int. J. Environ. Sci. Technol.* 13 (2016) 1065–1076, <https://doi.org/10.1007/s13762-016-0949-8>.
  - [38] L.M. Madeira, M.F. Portela, C. Mazzocchi, Nickel molybdate catalysts and their use in the selective oxidation of hydrocarbons, *Catal. Rev.* 46 (2004) 53–110, <https://doi.org/10.1081/CR-120030053>.
  - [39] J.A. Rodriguez, J.C. Hanson, S. Chaturvedi, A. Maiti, J.L. Brito, Phase transformations and electronic properties in mixed-metal oxides: experimental and theoretical studies on the behavior of NiMoO<sub>4</sub> and MgMoO<sub>4</sub>, *J. Chem. Phys.* 112 (2000) 935–945, <https://doi.org/10.1063/1.480619>.
  - [40] J.L. Brito, A.L. Barbosa, Effect of phase composition of the oxidic precursor on the HDS activity of the sulfided molybdates of Fe(II), Co(II), and Ni(II), *J. Catal.* 171 (1997) 467–475, <https://doi.org/10.1006/jcat.1997.1796>.
  - [41] A.A. Smirnov, Zh Geng, S.A. Khromova, S.G. Zavarukhin, O.A. Bulavchenko, A. A. Saraev, V.V. Kaichev, D.Yu Ermakov, V.A. Yakovlev, Nickel molybdenum carbides: synthesis, characterization, and catalytic activity in hydrodeoxygenation of anisole and ethyl caprate, *J. Catal.* 354 (2017) 61–77, <https://doi.org/10.1016/j.jcat.2017.07.009>.
  - [42] Y.V. Shubin, T.A. Maksimova, A.A. Popov, A.D. Varygin, A.D. Fedorenko, E. Y. Gerasimov, I.V. Mishakov, A.A. Vedyagin, Boosting effect of single-atom Sn on catalytic activity of Ni towards synthesis of carbon nanofibers from ethylene, *Appl. Catal. A Gen.* 670 (2024) 119546, <https://doi.org/10.1016/j.apcata.2023.119546>.
  - [43] J. Du, R. Zhao, Z. Zhu, A facile approach for synthesis and *in situ* modification of onion-like carbon with molybdenum carbide: synthesis and *in situ* modification of ion-like carbon with molybdenum carbide, *Phys. Stat. Sol. (a)* 208 (2011) 878–881, <https://doi.org/10.1002/pssa.201026646>.
  - [44] E.H. Martins Ferreira, M.V.O. Moutinho, F. Stavale, M.M. Lucchese, R.B. Capaz, C. A. Achete, A. Jorio, Evolution of the Raman spectra from single-, few-, and many-layer graphene with increasing disorder, *Phys. Rev. B* 82 (2010) 125429, <https://doi.org/10.1103/PhysRevB.82.125429>.
  - [45] A.C. Ferrari, J. Robertson, Raman spectroscopy of amorphous, nanostructured, diamond-like carbon, and nanodiamond, *Philos. Trans. R. Soc. Lond. Ser. A Math., Phys. Eng. Sci.* 362 (2004) 2477–2512, <https://doi.org/10.1098/rsta.2004.1452>.
  - [46] R.A. DiLeo, B.J. Landi, R.P. Raffaele, Purity assessment of multiwalled carbon nanotubes by Raman spectroscopy, *J. Appl. Phys.* 101 (2007) 064307, <https://doi.org/10.1063/1.2712152>.
  - [47] A. Weibel, D. Mesguich, G. Chevallier, E. Flahaut, C. Laurent, Fast and easy preparation of few-layered-graphene/magnesia powders for strong, hard and electrically conducting composites, *Carbon* 136 (2018) 270–279, <https://doi.org/10.1016/j.carbon.2018.04.085>.
  - [48] A.C. Ferrari, J.C. Meyer, V. Scardaci, C. Casiraghi, M. Lazzeri, F. Mauri, S. Piscanec, D. Jiang, K.S. Novoselov, S. Roth, A.K. Geim, Raman spectrum of graphene and graphene layers, *Phys. Rev. Lett.* 97 (2006) 187401, <https://doi.org/10.1103/PhysRevLett.97.187401>.
  - [49] A. Dychalska, P. Popielarski, W. Frankow, K. Fabisiak, K. Paprocki, M. Szybowicz, Study of CVD diamond layers with amorphous carbon admixture by Raman scattering spectroscopy, *Mater. Sci. -Pol.* 33 (2015) 799–805, <https://doi.org/10.1515/msp-2015-0067>.
  - [50] S.K. Jeng, D.S. Yu, Y.S. Kim, J. Ryou, S. Hong, C. Kim, S. Yoon, D.K. Efetov, P. Kim, S.H. Chun, Nanocrystalline graphite growth on sapphire by carbon molecular beam epitaxy, *J. Phys. Chem. C* 115 (2011) 4491–4494, <https://doi.org/10.1021/jp110650d>.

- [51] M. Pawlyta, J.-N. Rouzaud, S. Duber, Raman microspectroscopy characterization of carbon blacks: spectral analysis and structural information, *Carbon* 84 (2015) 479–490, <https://doi.org/10.1016/j.carbon.2014.12.030>.
- [52] T. Zhang, X. Yang, Q. Ge, CH<sub>4</sub> dissociation and C C coupling on Mo-terminated MoC surfaces: a DFT study, *Catal. Today* 339 (2020) 54–61, <https://doi.org/10.1016/j.cattod.2019.03.020>.
- [53] M. Figueras, R.A. Gutiérrez, H. Prats, F. Viñes, P.J. Ramírez, F. Illas, J. A. Rodríguez, Boosting the activity of transition metal carbides towards methane activation by nanostructuring, *Phys. Chem. Chem. Phys.* 22 (2020) 7110–7118, <https://doi.org/10.1039/D0CP00228C>.
- [54] S.D. Afonnikova, Y.I. Bauman, V.O. Stoyanovskii, M.N. Volochaev, I.V. Mishakov, A.A. Vedyagin, Effect of Cu on performance of self-dispersing Ni-catalyst in production of carbon nanofibers from ethylene, *C* 9 (2023) 77, <https://doi.org/10.3390/c9030077>.
- [55] Y.I. Bauman, Y.V. Rudneva, I.V. Mishakov, P.E. Plyusnin, Y.V. Shubin, D. V. Korneev, V.O. Stoyanovskii, A.A. Vedyagin, R.A. Buyanov, Effect of Mo on the catalytic activity of Ni-based self-organizing catalysts for processing of dichloroethane into segmented carbon nanomaterials, *Heliyon* 5 (2019) e02428, <https://doi.org/10.1016/j.heliyon.2019.e02428>.